Received: 10 November 2023 | Accepted: 8 June 2024

DOI: 10.1002/jmv.29752

RESEARCH ARTICLE

JOURNAL OF MEDICAL VIROLOGY WILEY

Metabolic and mitochondria alterations induced by SARS-CoV-2 accessory proteins ORF3a, ORF9b, ORF9c and ORF10

Blanca D. López-Ayllón[1] | Silvia Marin[2,3,4] | Marco Fariñas Fernández[2,5] | Tránsito García-García[6,7] | Raúl Fernández-Rodríguez[6,7] | Ana de Lucas-Rius[1] | Natalia Redondo[8,9] | Laura Mendoza-García[1] | Carles Foguet[10] | Juozas Grigas[11,12] | Alba Calvet[2,4] | José Manuel Villalba[13] | María Josefa Rodríguez Gómez[14,15] | Diego Megías[14] | Biagio Mandracchia[14,16] | Daniel Luque[14,17,18] | Juan José Lozano[3] | Cristina Calvo[19] | Unai Merino Herrán[1] | Timothy M. Thomson[3,19,20] | Juan J. Garrido[6,7] | Marta Cascante[2,3,4] | María Montoya[1]

[1]Viral Immunology Lab, Molecular Biomedicine Department, BICS Unit. Margarita Salas Center for Biological Research (CIB-CSIC), Madrid, Spain

[2]Department of Biochemistry and Molecular Biomedicine, Faculty of Biology, Universitat de Barcelona (UB), Barcelona, Spain

[3]CIBER of Hepatic and Digestive Diseases (CIBEREHD), Institute of Health Carlos III (ISCIII), Madrid, Spain

[4]Institute of Biomedicine of University of Barcelona (IBUB), University of Barcelona (UB), Barcelona, Spain

[5]Department of Biomedical Laboratory Science, Norwegian University of Science and Technology (NTNU), Trondheim, Norway

[6]Immunogenomics and Molecular Pathogenesis Group, UIC Zoonoses and Emergent Diseases ENZOEM, Department of Genetics, University of Córdoba, Córdoba, Spain

[7]Maimónides Biomedical Research, Institute of Córdoba (IMIBIC), Córdoba, Spain

[8]Unit of Infectious Diseases, University Hospital '12 de Octubre', Institute for Health Research Hospital '12 de Octubre' (imas12), Madrid, Spain

[9]Centre for Biomedical Research Network on Infectious Diseases (CIBERINFEC), Institute of Health Carlos III (ISCIII), Madrid, Spain

[10]British Heart Foundation Cardiovascular Epidemiology Unit and Victor Phillip Dahdaleh Heart and Lung Research Institute, University of Cambridge, Cambridge, UK

[11]Laboratory of Immunology, Department of Anatomy and Physiology, Lithuanian University of Health Sciences, Kaunas, Lithuania

[12]Institute of Microbiology and Virology, Lithuanian University of Health Sciences, Kaunas, Lithuania

[13]Department of Cell Biology, Physiology and Immunology, Agrifood Campus of International Excellence, University of Córdoba, Córdoba, Spain

[14]Scientific-Technical Central Units, Instituto de Salud Carlos III (ISCIII), Majadahonda, Spain

[15]Centro de Biología Molecular "Severo Ochoa" (CSIC-UAM), Universidad Autónoma de Madrid, Madrid, Spain

[16]ETSI Telecommunication, University of Valladolid, Valladolid, Spain

[17]Electron Microscope Unit, Mark Wainwright Analytical Centre, University of New South Wales, Sydney, Australia

[18]School of Biomedical Sciences, University of New South Wales, Sydney, Australia

[19]Barcelona Institute for Molecular Biology (IBMB-CSIC), Barcelona, Spain

[20]Translational Research and Computational Biology Laboratory, Faculty of Science and Engineering, Peruvian University Cayetano Heredia, Lima, Perú

Silvia Marin and Marco Fariñas Fernández have contributed equally to this work.

Juan J. Garrido, Marta Cascante and María Montoya have contributed equally to this work and share senior authorship.

Correspondence
María Montoya, Viral Immunology Lab, Molecular Biomedicine Department, BICS Unit. Margarita Salas Center for Biological Research (CIB-CSIC), Madrid, Spain.
Email: maria.montoya@cib.csic.es

Funding information
Spanish Ministry of Science project, Grant/Award Number: PID2021-123399OB-I00; Agency for Management of University and Research Grants from Generalitat de Catalunya-AGAUR, Grant/Award Numbers: 2020PANDE00048, 2021SGR00350; ICREA foundation (ICREA-Academia-2021 to MC) of Generalitat de Catalunya; AESi grant of the Instituto de Salud Carlos III, Grant/Award Number: PI20CIII-00014; Serra Húnter Fellow; Ramón y Cajal contract; CSIC's Global Health Platform (PTI+ Salud Global), Grant/Award Numbers: COVID-19-117, SGL2103015; Junta de Andalucía, Grant/Award Number: CV20-20089

Abstract

Antiviral signaling, immune response and cell metabolism are dysregulated by SARS-CoV-2, the causative agent of COVID-19. Here, we show that SARS-CoV-2 accessory proteins ORF3a, ORF9b, ORF9c and ORF10 induce a significant mitochondrial and metabolic reprogramming in A549 lung epithelial cells. While ORF9b, ORF9c and ORF10 induced largely overlapping transcriptomes, ORF3a induced a distinct transcriptome, including the downregulation of numerous genes with critical roles in mitochondrial function and morphology. On the other hand, all four ORFs altered mitochondrial dynamics and function, but only ORF3a and ORF9c induced a marked alteration in mitochondrial cristae structure. Genome-Scale Metabolic Models identified both metabolic flux reprogramming features both shared across all accessory proteins and specific for each accessory protein. Notably, a downregulated amino acid metabolism was observed in ORF9b, ORF9c and ORF10, while an upregulated lipid metabolism was distinctly induced by ORF3a. These findings reveal metabolic dependencies and vulnerabilities prompted by SARS-CoV-2 accessory proteins that may be exploited to identify new targets for intervention.

KEYWORDS
genome-scale metabolic modeling, metabolomics, mitochondria, ORF10, ORF3a, ORF9b, ORF9c, transcriptomics

1 | INTRODUCTION

Severe acute respiratory syndrome coronavirus 2 (SARS-CoV-2) is responsible for over 770 million cases of coronavirus disease 2019 (COVID-19) and over 7 million deaths since its emergence in 2019/2020.[1] Upon infecting susceptible cells, SARS-CoV-2 subverts and disables innate immune responses and, simultaneously, hijacks metabolic pathways to favor viral replication and production at the expense of the infected cell. Thus, metabolic reprogramming is the most consistent molecular change in SARS-CoV-2 infection.[2] Affected metabolic pathways including lipid metabolism, glucose metabolism, and oxidative phosphorylation have been observed in human patient samples, lung airway and alveolar organoids and metabolic models.[2–5] Focusing on lipid metabolism, an increased glycolysis and lipid accumulation[6] has been reported in patients together with a significantly decrease in fatty acids in plasma.[7] In the case of oxidative phosphorylation, mitochondria-related genes were found predominantly downregulated in nasopharyngeal infected cells.[8] Indeed, mitochondria has been observed to be in close contact with lipid droplets which were formed after cells were infected with the virus.[9] Although a complete mechanism explaining the development of all the aforementioned metabolic alterations in COVID-19 is yet to be proposed, viral-host protein interactions and the specific subcellular localization of various SARS-CoV-2 components help to identify potential sites and pathways leading to COVID-19 pathogenicity.

In particular, the mitochondrion, an organelle crucial for maintaining various metabolic functions, including energy metabolism and the production of reactive oxygen species (ROS), has emerged as a key target for SARS-CoV-2 activity, as indicated by an enrichment of viral dsRNA signal in mitochondria, coupled with mitochondrial lesions caused by SARS-CoV-2 infection.[10,11] Furthermore, changes in mitochondrial shape and structure, cristae reorganization and membrane potential disruption have been observed in SARS-CoV-2-infected cells.[10] The inhibition of mitophagy has been also shown with consequent accumulation of damaged mitochondria and augmented stress signaling by inhibiting microtubule-associated proteins 1 light chain or MAP1LC3 (hereafter referred to as LC3) binding,[11] a conjugation system required for the elongation and maturation of the autophagosome.[12] By contrast, another study suggests that ORF10 interacts with mitophagy receptor Nip3-like protein X (NIX) and LC3, in turn triggering mitophagy which hinders membrane-anchored antiviral signaling protein (MAVS)-mediated antiviral signaling.[13] In addition to their metabolic and bioenergetic functions, mitochondria play an integral role in host innate immune responses and interferon signaling. In particular, recognition of viral RNA by cytoplasmic sensors is followed by interaction with, and activation of MAVS.[14,15]

In addition to 4 main structural and 16 nonstructural proteins, the SARS-CoV-2 genome encodes 11 accessory proteins.[16,17] Although accessory proteins are considered to have a limited role in the replication and pathogenesis of the virus, multiple studies point

to their roles in immune response evasion strategies, interactions with metabolic pathways and induction of host cell apoptosis.[16,18,19] ORF3a, a membrane-associated protein and the largest SARS-CoV-2 accessory protein, has been reported to induce apoptosis in cell culture models[20] and to modulate host innate immune responses,[21] notably a suppression of IFN-I signaling via impeding signal transducer and activator of transcription 1 (STAT1) activation and nuclear translocation, resulting in increased suppressor of cytokine signaling 1 (SOCS1) levels.[21] A proposed role of ORF3a as a viroporin remains controversial.[22] Other SARS-CoV-2 accessory proteins, such as ORF10 and ORF9b, also suppress IFN-I responses, or antagonizes both IFN-I and IFN-III, respectively.[13,23] ORF9b inhibits the interaction between translocase of the outer membrane 70 (TOM70) and heat shock protein 90 (Hsp90), a critical step in the recruitment of the Hsp90/TANK-binding kinase 1 (TBK1)/interferon regulatory factor 3 (IRF3) complex within mitochondria.[18] This, in turn, leads to the suppression of antiviral gene transcription. ORF9c interacts with Sigma receptors, implicated in lipid remodeling and stress responses in the endoplasmic reticulum.[24] Also, ORF9b and ORF9c have been involved in inflammatory and fibrotic processes via interleukin-11 (IL-11).[25]

Prior evidence for SARS-CoV-2-induced metabolic and mitochondrial changes, and the putative functions ascribed to accessory proteins ORF3a,[26,27] ORF9b,[26,27] ORF9c[27] and ORF10[27,28] prompted us to investigate the potential for metabolic reprogramming by these ORFs. To this end, A549 human lung carcinoma cells were individually transduced with ORF3a, ORF9b, ORF9c and ORF10, analyzed for mitochondrial morphology, mass and function, and transcriptomic and metabolomic data generated to build genome-scale metabolic models (GSSM). We have found that SARS-CoV-2 accessory proteins ORF3a, ORF9b, ORF9c and ORF10 induced significant mitochondrial alterations and metabolic reprogramming. Further, GSMMs predicted both metabolic flux reprogramming features shared across all accessory proteins and specific ones for each accessory protein. These findings uncover metabolic dependencies and vulnerabilities that could be strategically leveraged for therapeutic purposes through the identification of potential intervention targets.

2 | RESULTS

2.1 | ORF3a induces a highly divergent transcriptome in A549 cells under equal basal growth conditions, as compared to ORF9b, ORF9c or ORF10

SARS-CoV-2 accessory proteins, ORF3a, ORF9b and ORF9c, have been shown to interact with mitochondria.[27,28] To further understand the consequences of expression of these proteins on mitochondrial function and cellular metabolism, ORF3a, ORF9b, ORF9c and ORF10 were individually transduced into A549 lung carcinoma cells (ORF-A549 cells) and drug-selected for stable constitutive expression of the viral genes and their expression confirmed by qRT-PCR and immunofluorescence (Figure 1B,C). Also, each individual ORF protein was detected by Western Blot (Supporting Information S1: Figure S1). As controls, nontransduced A549 cells and cells transduced with GFP only-expressing lentiviruses were used (A549 control cells). Both controls yielded equivalent results in all assays used throughout this study (data not shown).

To shed light on the biochemical pathways and biological processes modulated by ORF-A549 cells, a comparative transcriptomic analysis was performed. Unsupervised hierarchical clustering of all detectable transcripts showed that ORF3a-A549 cells displayed a clearly distinct transcriptome from control cells and from the rest of ORF-A549 cells (Supporting Information S1: Figures S2 and S3A). Transcriptomes of cells expressing ORF9b, ORF9c or ORF10 showed more similarity to each other and to control cells (Supporting Information S1: Figures S2 and S3A), although one-to-one comparisons of each ORF-A549 to control cell transcriptomes yielded a number of significant differentially expressed genes (DEGs) (Supporting Information S1: Figure S6 and Supporting Information S2: Table 1). Several transcripts significantly upregulated in ORF3a-A549 cells, but not in cells expressing the other three ORFs, were linked to innate immune functions, including interferon-regulated genes such as IFI44L, pattern-recognition receptors (PRRs) such as TLR5, or the complement and coagulation cascades, including VWA2, F5 or F13B (Supporting Information S2: Table 1). Likewise, a number of transcripts coding for proteins with metabolic functions were significantly overexpressed in these cells, including solute carrier family members (e. g., SLC9A9, SLC16A7, SLC16A9 or SLC25A27) and enzymatic metabolic regulators (e. g., ADH4 or ACSL5) (Supporting Information S2: Table 1). On the other hand, we observed a significant overlap of up- or downregulated DEGs among cells expressing ORF9b, ORF9c and ORF10 cells, with over 30% transcripts shared by each with the two other gene sets (Supporting Information S2: Table 1). Outstanding among the downregulated transcripts shared among cells expressing ORF9b, ORF9c and ORF10 cells, we found Stimulator of Interferon Response cGAMP Interactor 1 (STING1), accompanied with IFN signaling pathway genes such as IRF6, IFITM1 or IFITM3 in ORF9c-A549 cells or IFI44 or IFITM1 in ORF10-A549 cells, consistent with known functions exerted by these viral proteins as IFN-I and III signaling antagonists.[23,29,30]

We next resorted to gene-set expression analysis (GSEA)[31] to gain a broader perspective of biochemical pathways and cellular processes perturbed by the expression of these viral accessory proteins (Supporting Information S1: Figure S3B-E). Metabolic pathways revealed that ORF3a, but not the other ORFs, induced significant changes in the biliary acid pathway and underrepresentation of mTORC1, hypoxia, glycolysis, oxidative phosphorylation (OXPHOS) or mitochondrial ROS pathways (Supporting Information S1: Figure S2B). Representative genes involved in the six more significant metabolic enrichment pathways altered by ORF3a expression were represented in Supporting Information S1: Figure S4, and a selected cluster of genes was shown in Figure 2A. As a representative of the biliary acid pathway, we verified by qRT-PCR ACSL5 overexpression in ORF3a-A549 cells, but not in cells expressing the other ORFs (Figure 2B).

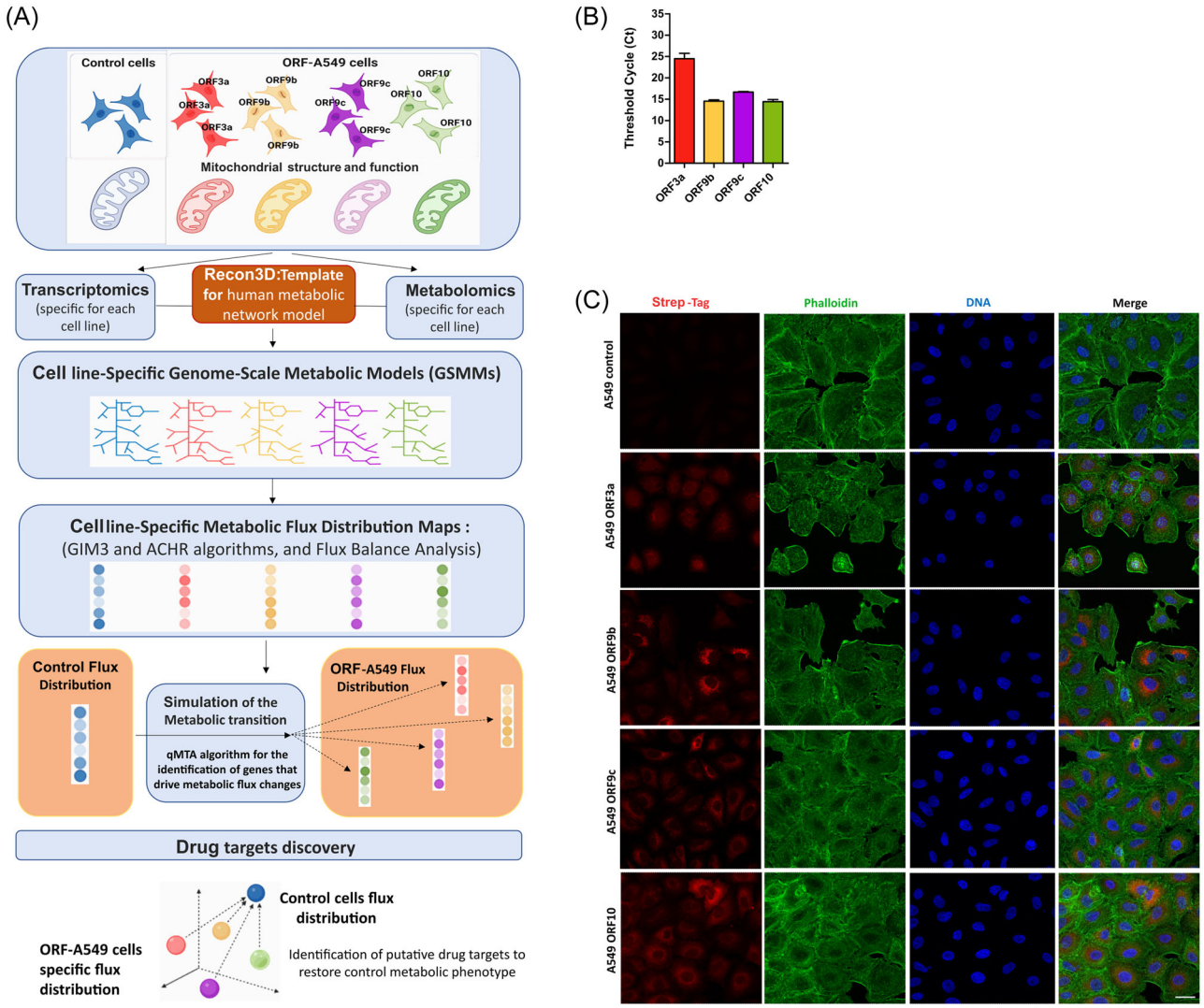

FIGURE 1 (A) Experimental workflow. Image generated in Biorender. (B) Threshold cycle (Ct) of SARS-CoV-2 ORF3a, ORF9b, ORF9c or ORF10 viral genes. (C) Representative confocal images of A549 cells expressing SARS-CoV-2 ORF3a, ORF9b, ORF9c or ORF10 accessory proteins (objective 63×, scale bar 25 μm).

The underrepresentation of the OXPHOS pathway induced by ORF3a prompted us to conduct a more detailed examination of genes coding for mitochondrial electron transport chain (ETC) components and cristae morphology and function. GSEA with an ETC-focused gene set showed a significant underrepresentation in cells expressing ORF3a, but not the other three ORFs (Figure 3). This was due to the ORF3a-induced downregulation of genes for components of ETC complexes I, III, IV and V (Figure 3A). As such, ORF3a may play a prominent role in the downregulation of mitochondrial genes and functions reported upon SARS-CoV-2 infection of lung epithelial cells.[5] By contrast, ORF9b, ORF9c and, particularly, ORF10, induced an upregulation of genes for ETC, albeit without reaching significance in terms of pathway representation by GSEA (Supporting Information S1: Figure S5). Expression analysis of genes for mitochondrial cristae morphology and function also indicated a downregulation by ORF3a of genes for critical cristae regulators, including OPA1, SAMM50, TOMM40 and components of the mitochondrial contact site and cristae organizing system (MICOS), MIC60 (IMMT) and MIC13 (MICOS13) (Figure 3B). Once again, ORF9b, ORF9c and ORF10 displayed transcriptional profiles for mitochondrial cristae factor components that were converse to those induced by ORF3a, with upregulation of OPA1, SAMM50 or TOMM40 and downregulation of APOO (MIC26), APOOL (MIC27) or ATP5MF, particularly by ORF10 (Figure 3B), although ATP5MF was not downregulated by ORF9c.

2.2 | ORF3a and ORF9c induce significant structural alterations in mitochondria

Given the effect observed on OXPHOS, ETC and mitochondria morphology-related genes induced by ORF3a, mitochondrial membrane potential ($\Delta\psi_m$) was analyzed by flow cytometry using

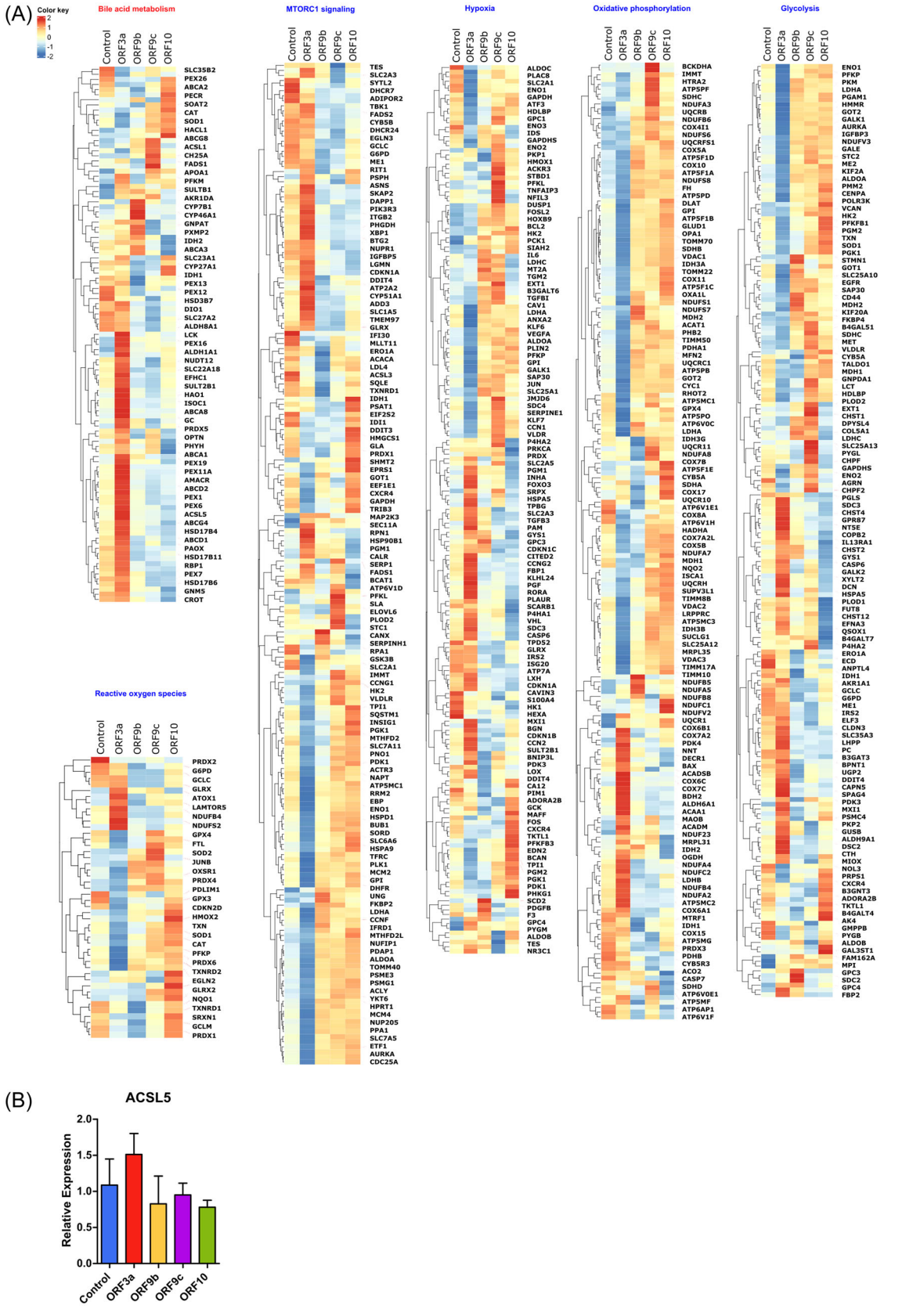

FIGURE 2 (A) Representative genes involved in metabolic enrichment pathways altered by ORF3a expression. The six more significant metabolic pathways upregulated (red) and downregulated (blue) altered by ORF3a expression are represented. Gene expression pattern of each pathway in all A549 transduced cells and A549 control cells was compared. The color key corresponds to row-normalized values of Log2FC. (B) Relative expression of bile acid metabolism gene ACSL5 validated by qPCR.

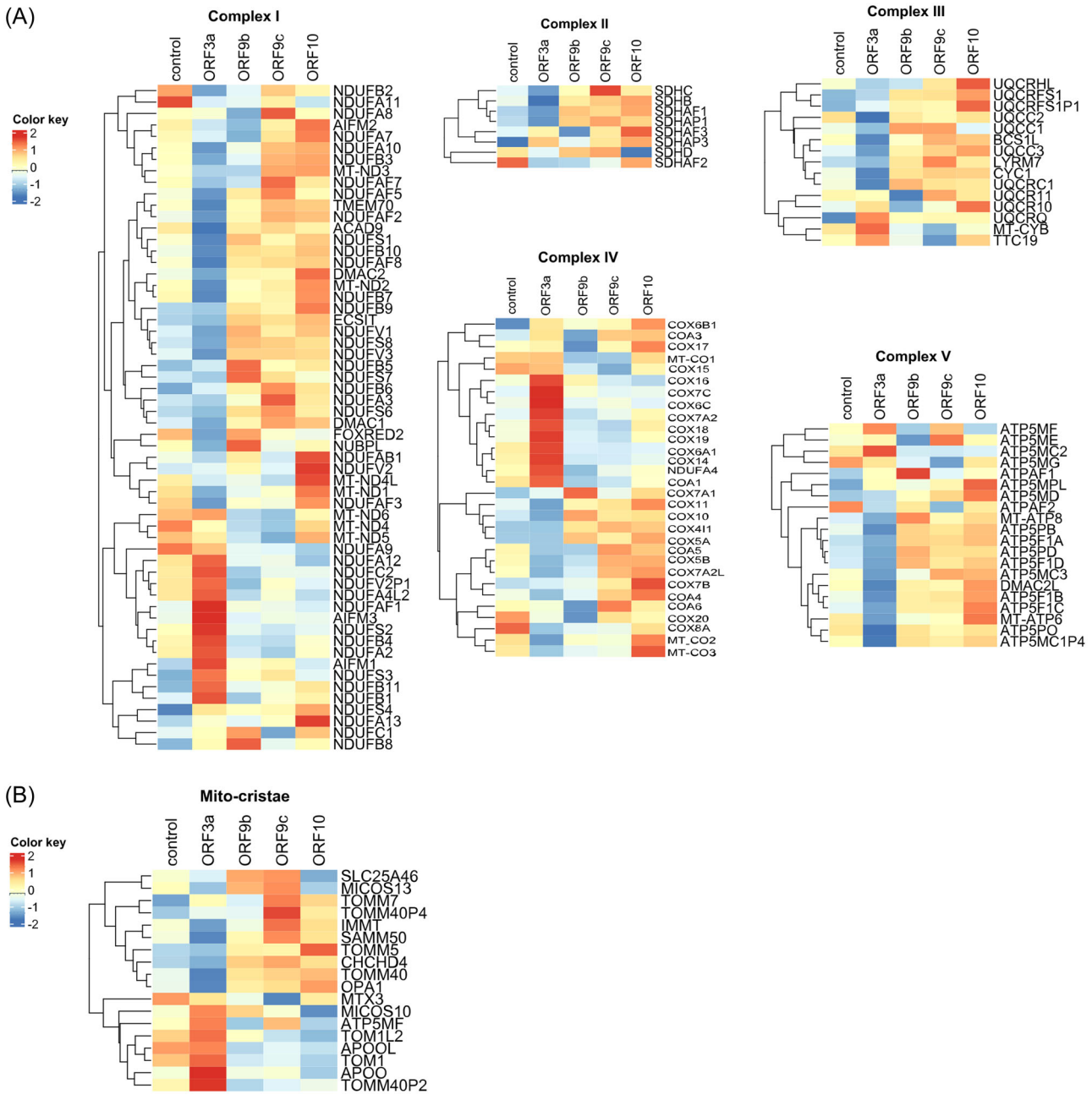

FIGURE 3 Electron transport chain (ETC) and mitochondrial cristae gene expression in A549 cells transduced with SARS-CoV-2 ORF3a, ORF9b, ORF9c or ORF10 accessory proteins. Heatmaps of DEGs related with mitochondrial complexes (I–V) (A) and mitochondria critae (Mito-cristae) (B) in A549 transduced cells compared with A549 control cells. The color key corresponds to row-normalized values of Log2FC.

MitoView 633[32] (Figure 4A and Supporting Information S1: Figure S7). Two populations were defined according to their mitochondrial membrane potential: high-activity and low-activity mitochondria. Indeed, ORF3a-A549 cells exhibited a significantly higher number of low-activity mitochondria in their cytoplasm. These results suggest that the downregulated expression observed in these cells may affect the mitochondrial membrane potential. ORF10-A549 cells also showed an increase in this mitochondrial population, although without reaching statistical significance (Figure 4A).

It is worth noting that the size of mitochondria was significantly smaller in all ORF-transduced cells, compared to control cells, being particularly evident in ORF3a-A549 and ORF9b-A549 cells (Figure 4B), suggesting an augmented mitochondrial fission. Moreover, ORF-A549 cells showed an increased number of mitochondria compared to control cells, although in the case of ORF3a-A549 it was not statistically significant (Figure 4C), and the total cell area covered by mitochondria (mitochondrial mass) was smaller in all four ORF-A549 cells versus control cells (Figure 4D,E). Noteworthy,

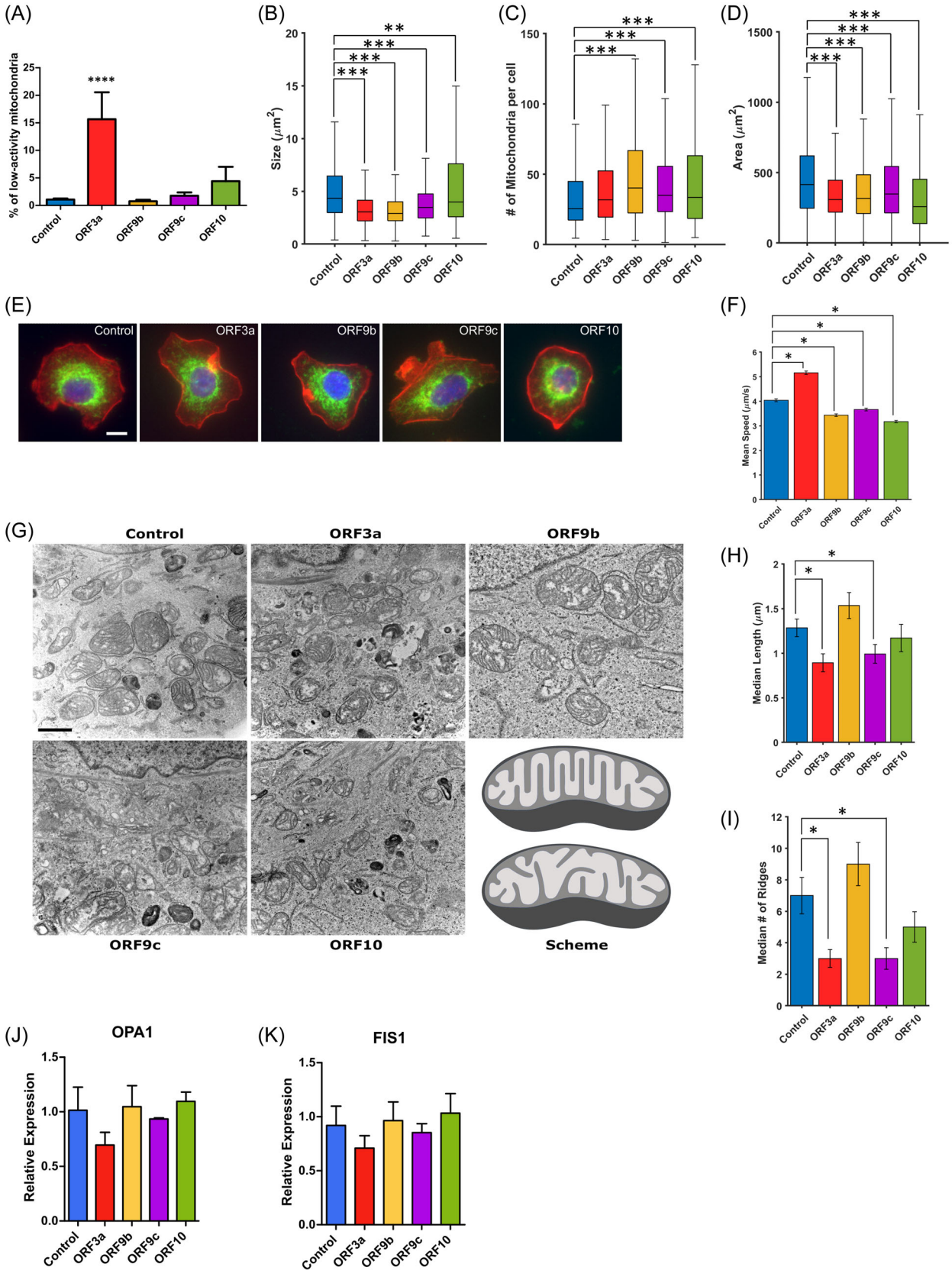

FIGURE 4 (See caption on next page).

ORF10-A549 cells exhibited bigger mitochondria than other transduced cell lines, but the area covered by them was the smallest of all ORF-A549 cells. This result may suggest a more compact mitochondrial area, which hinders an accurate individual mitochondria determination.

As mitochondrial morphology, function and motility are coupled[33,34] a study of mitochondrial motility was next performed by live-cell imaging. Based on their motility, two subpopulations of motile mitochondria were observed in all cell lines, namely low- (<4 μm/s) and high-speed (≥4 μm/s) mitochondria (Supporting Information S1: Figure S8). Analysis of mitochondrial motion showed significant differences among the different ORF-expressing cells (Figure 4F). In ORF3a-A549 cells, the number of mitochondria traveling at high speed was significantly higher than in control cells, and the number of mitochondria at low speed was lesser. By contrast, in the rest of ORF-A549 cells, the mean speed of mitochondria traveling was significantly lower than in control cells (Figure 4F and Supporting Information S1: Figure S8).

Ultrastructural analysis by transmission electron microscopy showed a shorter mitochondria length in all ORF-A549 cells as compared to control cells, except in ORF9b-A549 (Figure 4G,H, Supporting Information S1: Figures S9 and S10). This decrease in mitochondrial length was significant in the case of cells expressing ORF3a and ORF9c. Moreover, a significantly lower average number of ridges was observed in these cells (Figure 4I, Supporting Information S1: Figures S9 and S10), conforming less organized cristae with a loss of parallelism (cristae aligned in the same orientation) and more hollow mitochondria than in control cells (Figure 4G, Supporting Information S1: Figures S9 and S11). These abnormal cristae morphologies are consistent with altered expression of cristae-related genes, although likely involving different mechanisms between ORF3a-A549 and ORF9b-A549 cells, since they showed distinct gene expression patterns (Figure 3B). Interestingly, although ORF9b induced a significant population of smaller mitochondria (mitochondrial fragmentation or fission) (Figure 4B), the median diameter of mitochondria was larger (Figure 4H). It is possible that a more rounded shape of the mitochondria may cause them to appear erroneously larger in longitudinal sections. Consistent with these results, OPA1, a major determinant of mitochondria cristae morphology and remodeling and inner mitochondrial membrane fusion,[35–37] was selectively downregulated in ORF3a-A549 cells, as determined by RNA-seq (Figure 3B) and qRT-PCR (Figure 4J). Intriguingly, FIS1, a promoter of mitochondrial fission,[38–40] was also downregulated in ORF3a-A549 cells (Figure 4K), in spite of the observed enhanced mitochondrial fission. In this regard, although FIS1 is a major recruiter of DRP1 to the mitochondrial outer membrane to execute fission, its silencing does not elongate mitochondria in all cell types[41,42] and human DRP1 can be recruited by other mitochondrial membrane–anchored proteins, particularly MFF,[41,43–48] and, as such, downregulation of FIS1 in our system does not necessarily counter our morphological observations.

In summary, ORF3a favors mitochondrial fission and altered cristae architecture, coupled to diminished $\Delta\psi_m$ and enhanced motility in a significant population of mitochondria. On the other hand, ORF9c, while causing mitochondrial fission and ultrastructural alterations similar to those induced by ORF3a, did not cause loss of $\Delta\psi_m$ or enhanced mitochondrial motility. Finally, ORF9b induced a marked mitochondrial fragmentation, while ORF10 promoted mitochondrial fusion.

2.3 | ORF9b and ORF9c overexpression causes the strongest mitochondrial function alteration

Mitochondria are major source of ROS, and excessive ROS production leads to oxidative damage that impairs the ability of mitochondria to generate ATP and perform metabolic functions.[49] Given the above evidence of impact of the four accessory proteins on mitochondrial morphology and gene expression, ROS levels were measured with the cell-permeant H2DCFDA probe. A549 cells expressing ORF9c and ORF10 exhibited a significant increase in ROS levels compared to control cells (Figure 5A), whereas a slight increment was detected in cells expressing ORF9b ($p = 0.0507$). In contrast, a modest reduction was observed in ORF3a-A549 cells compared to control (Figure 5A).

To determine the functional consequences of SARS-CoV-2 accessory proteins on cellular bioenergetics, oxygen consumption rate (OCR), which represents the rate of OXPHOS, was measured (Figure 5B). Maximal respiration was significantly reduced by all four viral proteins, since basal respiration and ATP production were significantly impaired only by ORF3a, ORF9b and ORF9c (Figure 5C). Moreover, spare respiratory capacity was significantly hampered by ORF9b, ORF9c and ORF10, but not by ORF3a.

FIGURE 4 Mitochondrial morphology and diffusion in ORF-A549 cells. (A) Quantification of the percentage of low-activity mitochondria in ORF-A549 cells stained with MitoView 633. Data are represented as mean ± SD ($n = 4$). (B–E) Box and whisker plots showing the distributions of mitochondrial size (mitochondria fragmentation) (B), number per cell (C), and area covered by mitochondria (mitochondrial mass) (D). At least 200 cells were analyzed. (E) Representative images of the datasets used to generate the distributions in (B–E). Mitochondria are marked in green (TOM20), nuclei in blue (DAPI), and actin in red (Phalloidin). Scale bar: 10 μm. (F) Mean speed of the tracked mitochondria measured for each cell line. (G) Analysis by transmission electron microscopy of mitochondrial appearance in ORF-A549 cells ultrathin sections. Scale bar indicates 1 μm. Last panel shows a schematic representation of mitochondria with organized and parallel mitochondrial ridges (top), and mitochondria with disorganized, nonparallel mitochondrial ridges and hollowed out areas (bottom). Median of mitochondria longest diameter (H) and median number of ridges per mitochondrion (I) evaluated from TEM micrographs of each cell line. In both cases (H and I), at least 50 mitochondria were analyzed. Mitochondrial dynamics related genes OPA1 (J) and FIS1 (K) were validated by qPCR. Statistical significance is as follows: $^{*}p < 0.05$, $^{**}p < 0.01$, $^{***}p < 0.001$, $^{****}p < 0,0001$.

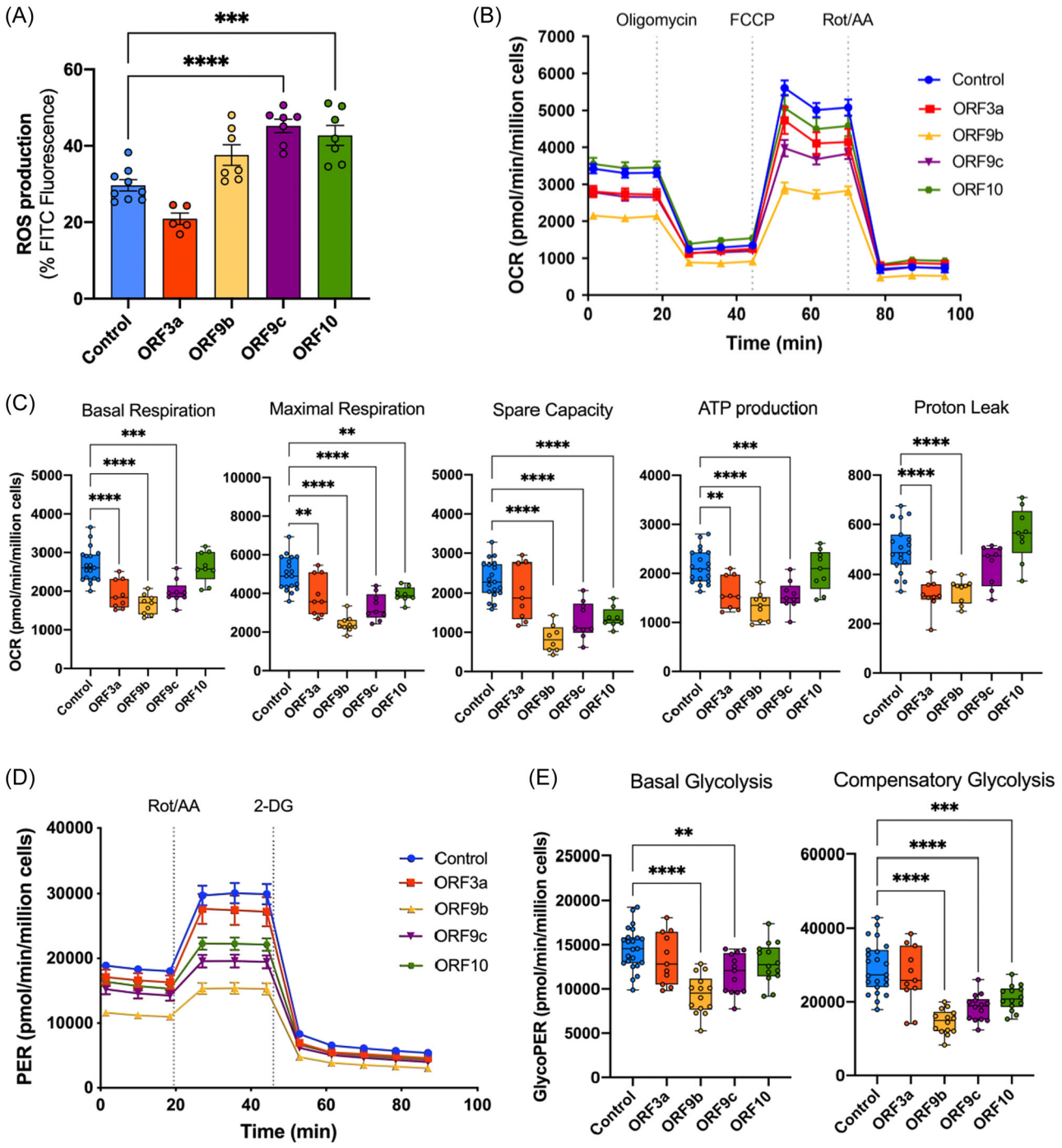

FIGURE 5 Respiratory and glycolytic profiles of A549 cells expressing SARS-CoV-2 accessory proteins. (A) ROS production measured by flow cytometry in A549 cells expressing SARS-CoV-2 ORF3a, ORF9b, ORF9c or ORF10 and control cells. (B) Seahorse XF Mito Stress test profile of oxygen consumption rate (OCR) in control and transduced cells. (C) Box and whisker plots showing the normalized basal respiration, maximal respiration, spare respiratory capacity, ATP production and proton leak in control and transduced cells. (D) Seahorse XF Glycolytic Rate test profile of proton efflux rate (PER). (E) Box and whisker plots showing the normalized basal and compensatory glycolytic PER. Horizontal line represents the mean and points individual replicates. Statistical significance is given as follows: $^{*}p < 0.05$, $^{**}p < 0.01$, $^{***}p < 0.001$ and $^{****}p < 0.0001$.

Interestingly, basal and maximal respiration, spare respiratory capacity and ATP production were strongly reduced by ORF9b, suggesting that this protein compromises the ability of cells to respond to high respiratory demands or to acute stress (Figure 5C). Both ORF3a and ORF9b induced, to similar degrees, significantly decreased level of proton leak (Figure 5C). These results suggest different effects of the four accessory proteins on mitochondrial function, which was particularly marked in the case of ORF9b.

Further, glycolytic rate assays were performed to monitor basal and compensatory glycolysis in ORF-A549 cells. Figure 5D shows proton efflux rate (PER) results converted from OCR and extracellular acidification rate (ECAR) data. ORF9b and ORF9c caused significantly reduced basal and compensatory glycolysis compared to control cells, whereas ORF10 only induced a decrease in compensatory glycolysis (Figure 5E). These results suggest that cells expressing ORF9b, ORF9c and ORF10, but not ORF3a, fail to resort to glycolysis to compensate for the observed defects in OXPHOS. In contrast, ORF3a-A549 cells showed basal and compensatory glycolysis similar to control cells, suggesting that these cells, but not those expressing ORF9b, ORF9c or ORF10, have developed glycolytic compensatory mechanisms[50] to offset the diminished mitochondrial ATP production.

Overall, our results indicate that all four ORFs were involved in mitochondrial dysfunction, which was particularly severe as a consequence of ORF9b expression, and, to a lesser extent ORF9c expression. However, only ORF3a resorted to glycolysis to counteract accessory protein-induced deficits in mitochondrial energy production.

2.4 | Genome-scale metabolic flux maps unveil common and private metabolic alterations induced by ORF3a, ORF9b, ORF9c and ORF10

Subsequently, GIM3E[51] and quadratic metabolic transformation algorithms (qMTA)[52] were used to integrate uptake and production rates of metabolites (Supporting Information S3: Table 2), respiration data and transcriptomics to simulate condition-specific flux maps (genome-scale metabolic models, GSMM) for the major four metabolic superfamilies. Notably, ORF3a had a major impact on cell bioenergetics, carbohydrate metabolism and cofactors, and nucleotide metabolic pathways superfamilies, whereas ORF9b altered mostly amino acid metabolism and lipid metabolism (Figure 6A). On the other hand, detailed individual metabolic pathway analysis (Figure 6B) revealed distinctive disruptions caused by ORF3a and ORF10. Pathways uniquely overrepresented in ORF3a-A549 cells were inositol phosphate, ether lipid, phosphonate-phosphinate, vitamin B6, glycerophospholipid metabolism and nicotinate-nicotinamide metabolism, consistent with the above-described enrichment in bile acid biosynthetic pathways and peroxisome biogenesis, where many of these processes take place,[5] as well as essential amino acid metabolism (histidine, phenylalanine and tyrosine). Moreover, ORF3a-A549 cells displayed a distinctive decrease in fatty acid metabolism-related pathways, glycolysis, OXPHOS, metabolism of steroid hormones, arginine, proline citrate, one carbon, pentose phosphate, and purine metabolism, as suggested above by transcriptomic analysis. ORF10-A549 cells displayed a strong decrease in lysine degradation and histidine metabolism, in contrast to the slight increase observed for ORF3a-A549 cells. ORF10 also induced a modest but distinctive increase in one-carbon and fatty acid metabolism-related pathways, amino acid metabolism (phenylalanine, tyrosine, tryptophan, glycine, threonine and arginine), and the citrate cycle (Figure 6B). ORF9b-A549 and ORF9c-A549 cells shared several metabolic communalities, including a generalized decrease in fatty acids, ketone bodies and amino acid metabolism, and increased sphingolipid metabolism. Interestingly, these two ORFs had similar effects on lipid metabolism-related pathways, and induced a marked decrease in amino acid metabolism, particularly evident in ORF9b-A549 cells (Figure 6B). Intriguingly, a common feature shared by all four ORF-A549 cells was a decrease in steroid biosynthesis pathways as compared to control cells.

Several studies have assessed the metabolic consequences of SARS-CoV-2 infection in lung epithelial cells lines.[53–55] To analyze whether the metabolic alterations induced by individual SARS-CoV-2 accessory proteins are paralleled by SARS-CoV-2 infection, transcriptomic data from Blanco-Melo et al., 2020 [53] were subjected to GSEA so as to assess enrichment in metabolic pathways in SARS-CoV-2 infected Calu-3 and A549-ACE2 cells. Comparison of normalized enrichment scores (NES) between control and infected cells revealed a downregulation of metabolic pathways in infected cells that paralleled several of those altered by expression of individual ORFs in A549 cells (Figure 6C). This suggests that SARS-CoV-2 accessory proteins may play significant roles in the metabolic reprogramming ensuing infection by the complete virion.

According to these results, expression of several genes related with such pathways was analyzed. Cytidine diphosphate diacylglycerol synthases (CDS enzymes) are critical for maintaining phosphoinositide levels during phospholipase C (PLC) signaling [56] and cardiolipin synthesis.[56] CDS1 enzyme regulates the amount of phosphatidylinositol available for signaling, and it determines the size of lipid droplets.[56] Thus, it has an important role in glycerophospholipid metabolism. Here, we found CDS1 overexpressed in ORF3a-A549 and downregulated in ORF9c and ORF10-A549 cells (Figure 6D). On the other hand, PLPP1 is also involved in glycerophospholipid metabolism and ether lipid metabolism pathways [57] PLPP1 it was also found upregulated in ORF3a cells, and mainly downregulated in ORF9c transduced cells (Figure 6E). ALDH7A1 was recently found to play a significant role in protecting mammalian cells from hyperosmotic stress, and it is enzymatically active against a number of lipid peroxidation-derived aldehydes which are formed under oxidative conditions.[58] Hyperosmotic stress is coupled to the generation of ROS and elevated oxidative stress within the cell.[59] Here, we did not observe significant changes in ALDH7A1 in ORF3a and ORF9b expressing cells, whereas it was downregulated in ORF9c and ORF10 transduced cells (Figure 6F). These results correlate with the ROS production values observed in these cells (Figure 5A), and it might indicate that ALDH7A1 protects ORF3a and ORF9b transduced cells under oxidative conditions.

2.5 | Identification of putative targets to counteract the metabolic reprogramming induced by ORF3a and ORF10

To explore potential targets for pharmacological intervention, the quadratic metabolic transformation algorithm (qMTA) (https://github.com/cfoguet/cobrafunctions) was applied to simulate gene knock

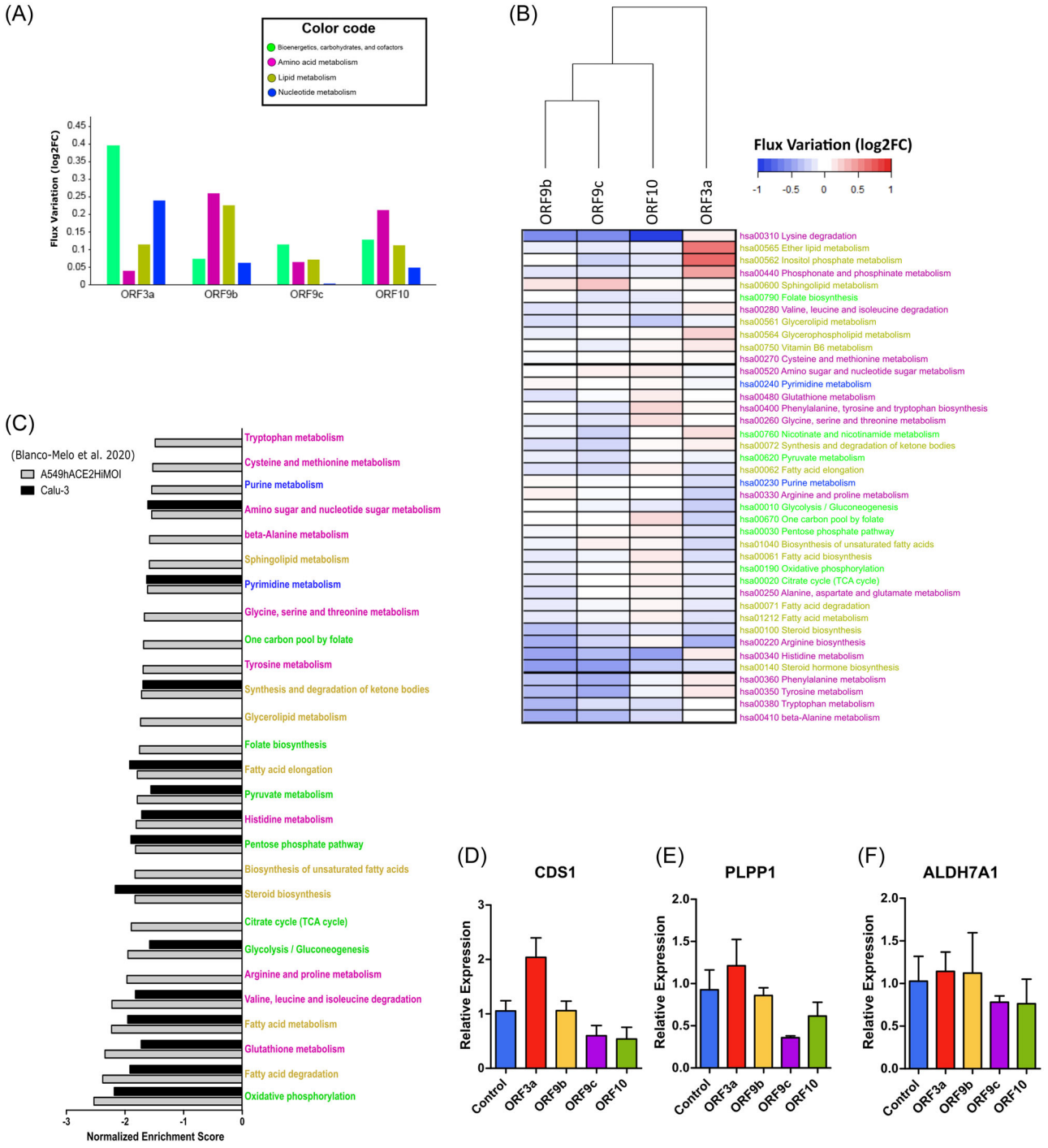

FIGURE 6 Metabolic flux changes induced by ORF3a, ORF9b, ORF9c, and ORF10 relative to control cells. (A) Flux variation within metabolic superfamilies. Metabolic fluxes were expressed as log2 FC of ORF-A549 versus control cells. (B) Heatmap representing flux modulation of ORF-A549 cells for metabolic individual KEGG pathways. (C) Normalized enrichment score (NES) comparison for metabolic individual KEGG parhways in Calu-3 and A549ACE2HiMOI cell lines generated in Blanco-Melo et al., 2020.[53] The pathways represented correspond with those found in (B). Color code corresponds to metabolic superfamilies represented in (A). Lipid metabolism related genes CDS1 (D), PLPP1 (E) and ALDH7A1 (F) were validated by qPCR.

downs (KDs) with the potential to revert the metabolic reprogramming induced by each individual SARS-CoV-2 accessory protein. For each cell line, two KDs were chosen among the ten targets (Figure 7) predicted to be the most effective for reverting the observed metabolic phenotypes. Each outcome was linked to an existing drug, when possible. The inherent design of this approach, based on gene loss simulations, only allows to predict pathway perturbation reversal in association with drugs with inhibitory functions. As such, as most of the metabolic pathways perturbed by ORF9b and ORF9c showed a decreased representation (Figure 6B), no significant drugs were

predicted to revert such alterations by in silico simulation. The best-inferred targets for reverting the metabolic perturbations induced by ORF10 were dihydrolipoamide dehydrogenase (DLD), a component of the oxoglutarate dehydrogenase complex, and SLC25A10, a transporter responsible for transferring TCA-cycle metabolites like succinate, fumarate, or malate from the mitochondria to the cytosol (Figure 7).

On the other hand, phospholipase D2 (PLD2) and phospholipase C beta-1 (PLCB1) were the highest scoring targets whose inhibition or absence is predicted to revert specific metabolic perturbations induced by ORF3a. As such, targeting either of these two enzymes is expected to revert alterations in several pathways related to lipid metabolism, such as "inositol phosphate metabolism", "ether lipid metabolism", "glycerophospholipid metabolism" or "phosphonate and phosphinate metabolism" (Figure 7). PLD2 hydrolyzes glycerophospholipids to produce phosphatidic acid, which can subsequently be converted into lysophosphatidic acid (LPA) and diacylglycerol (DAG). Indeed, the activity of PLD is known to influence the ability of viruses to enter and replicate in mammalian cells. For instance, infection of respiratory epithelial cells with influenza virus has been reported to stimulate PLD activity and chemical inhibitors of PLD2, RNAi depletion of PLD2 and pretreatment with primary alcohols can mitigate the infectivity of viral particles and also the viral titer produced postinfection.[60] Importantly, coronavirus envelopes are particularly enriched in ether phospholipids, along with cholesterol and sphingolipids,[61] with a lipid composition distinct from the plasma membrane. Therefore, inhibiting phospholipases that catalyze the production of ether phospholipid precursors may impair the formation of viral envelopes. On the other hand, PLCB1 catalyzes the hydrolysis of 1-phosphatidylinositol 4,5-bisphosphate into DAG and inositol 1,4,5-trisphosphate (IP3). Therefore, the target prediction by qMTA is in consonance with the above predictions independently reached by GSEA and GSMMs, thus reinforcing the conclusion that ORF3a causes the upregulation of these pathways, which may underlie at least some of the observed phenotypes.

To test this prediction ORF3a-A549 cells were treated for 24 h with 1 μM of the PLD2 inhibitor CAY10594. After treatment, mitochondrial morphology and differential gene expression were analyzed. This inhibitor was able to restore to control levels the median mitochondria diameter and the number of ridges per

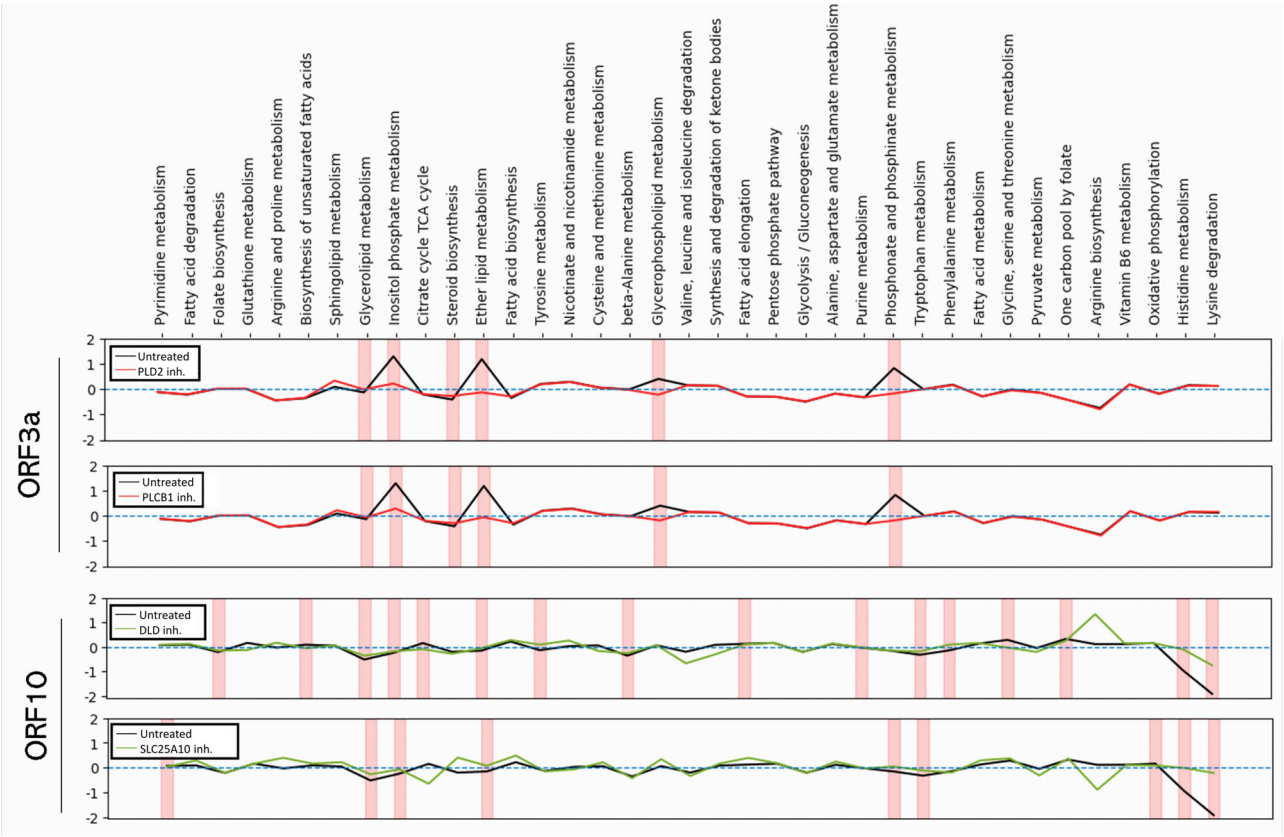

FIGURE 7 Metabolic pathway analysis representing the two-best metabolic-reversing drugs from ORF3a-A549 and ORF10-A549 cells towards the control A549 cells resting state. Each graph displays a comparison between the metabolic profile triggered by the viral protein transduction (black line), and its reversion by *in silico* chosen drug-gene knock downs (50% KD) selected from GSMM-mediated *in silico* analysis (red line in ORF3a, and green line in ORF10). Each line represents the metabolic change of either an ORF expression, or an ORF expression + drug, versus control cells. Pink bars mean metabolic alterations in the pathways represented, and black line peaks show the most dramatic ones. Y axis represents log2 FC, and the dashed-horizontal blue line at each plot represents the control state (i.e., log2 FC = 0). DLD, dihydrolipoamide dehydrogenase; PLD2, phospholipase D2; PLCB1, phospholipase C beta-1; SLC25A10, Solute Carrier Family 25 Member 10.

mitochondrion in ORF3a-A549 cells (Figure 8A–C). These results agree with other studies, which showed an improvement in mitochondrial quality and quantity after PLD pharmacoinhibition.[62] Integration of transcriptomics data into treatment-specific GSMM to simulate the effect of CAY10594 inhibitor on ORF3a-A549 cells metabolic flux distribution, showed that alterations on the major lipid superfamilies induced by ORF3a are partially reverted by the PLD2 inhibitor (Figure 8D, bottom panel). Moreover, the overall flux map obtained after CAY10594 treatment is closer to the control cells flux reference values than the ORF3a-A549 cells flux map, which is indicative of a recovery of the metabolic landscape of ORF3a-A549 cells induced by the PLD2 inhibitor (Figure 8D).

3 | DISCUSSION

Insights into mechanisms of SARS-CoV-2 viral life cycle and pathogenic effects are facilitated by a large number of studies of viral-host protein-protein interactions producing comprehensive interactome maps,[19,24,63] as well as a comprehensive GSMM of SARS-CoV-2 infected cells.[2] However, the impact of individual accessory proteins on host cell metabolic pathways remains unknown. In this study, we show that the individual expression of the SARS-CoV-2 accessory proteins, ORF3a, ORF9b, ORF9c or ORF10, in A549 lung epithelial cells results in significant mitochondrial and metabolic alterations, some of which are distinctive of a particular accessory protein. The estimation of metabolic flux changes induced by these accessory proteins, inferred from GSMMs, are in accordance with the results of these metabolic functional assays that are presented in detail in Supporting Information S3: Table 2 (metabolite exchange fluxes) and in Figure 5 (oxygen consumption and mitochondrial function changes). Furthermore, by combining transcriptomic analysis with functional and metabolic data in accessory protein-specific GSMMs, several alterations were identified that may point to a putative target for investigating novel therapies.

A salient outcome of our study is that, despite the distinct metabolic reprogramming caused by each of the accessory proteins studied, particularly ORF3a, all four proteins caused altered mitochondrial features. These results are consistent with others studies that describe the interaction of these accessory proteins with mitochondria.[27,28]

Mitochondria are internally organized into cristae, which are fundamental structures whose shape changes under different physiological conditions.[64] The shape of the cristae is determined by the interaction of mitochondrial shape proteins,[65,66] and perturbing such proteins disrupt cristae shape and change cristae-located OXPHOS system, which affects cellular growth and metabolism. Interactions between SARS-CoV-2 accessory proteins and host cell mitochondria have been proposed by multiple studies.[10,11,13,67] Morphological changes in shape, size, cristae reorganization and cell location have been shown in mitochondria of SARS-CoV-2-infected cells.[10,67] Here, we have outlined the accessory viral proteins involved. Our findings indicate that the presence of ORF3a, ORF9c, and ORF10 results in alterations in both the shape and quantity of cristae. Cells expressing ORF3a, despite having smaller mitochondria and ridges, increased mitochondrial movement (Figure 4F and Supporting Information S1: Figure S7) and decreased ROS levels (Figure 5A). In these cells, MIC60 (IMMT) and OPA1 downregulation, which also plays a role in cristae remodeling,[68] may explain the disruption of mitochondrial cristae organization observed in our study. ORF9c-expresing cells, in addition to having smaller mitochondria, showed a significant increase in ROS levels (Figure 5A). For this reason, they may be unable to compensate the structural alterations observed and showed altered mitochondrial function, but less marked than cells expressing ORF9b (Figure 5B,C). Unlike ORF3a expressing cells, ORF9c transduced cells were unable to compensate that dysfunction by increasing glycolysis (Figure 5D,E). In contrast to ORF3a, ORF9c has not been found to interact with mitochondrial factors essential for the biogenesis and maintenance of cristae, and thus its expression is not predicted to disrupt the structure of cristae to the same extent as ORF3a. This suggests that these ORFs may potentially impact either the mitochondrial shaping proteins or even the mitochondrial oxidative system itself. Genes for mitochondrial proteins that determine the shape, length and function of mitochondrial cristae,[65,69] are variously downregulated by the accessory proteins studied here, particularly by ORF3a, which caused a significant downregulation in mitochondria dynamics related genes, such as OPA1. The other accessory proteins caused a downregulation of different sets of genes for proteins that also play important roles in mitochondrial and cristae morphology, suggesting that different accessory proteins disrupt mitochondrial morphology and function through different mechanisms. All four accessory proteins induced mitochondria size reduction (mitochondria fragmentation), which was compensated by an increase in the total number of mitochondria, that can barely equal mitochondrial mass found in control cells. Interestingly, although ORF9b induced a significant population of smaller mitochondria (mitochondrial fragmentation or fission), the median diameter of mitochondria was larger. It is possible that a more rounded shape of the mitochondria may cause them to appear artifactually larger in longitudinal sections. Collectively, these observations are in agreement with previous studies showing mitochondrial morphological alteration and/or destabilization of normal physiological fission–fusion dynamics ensuing SARS-CoV-2 infection[10] and suggest that such perturbations may be caused, at least partly, by these accessory proteins. Other processes, such as disruption of mitophagy as reported for ORF10,[11,13] may also contribute to the size and shape changes in mitochondria upon viral infection, due either to excessive sequestration of healthy mitochondria or to accumulation of damaged mitochondria.

Whether a cause or a consequence of specific morphological changes in mitochondria triggered by SARS-CoV-2 and its accessory proteins studied here, they are associated with distinct metabolic and functional perturbations. As such, consistent with studies demonstrating an increased production of ROS in SARS-CoV-2 infected cells,[11] we have shown that ORF9c and ORF10 induce increased

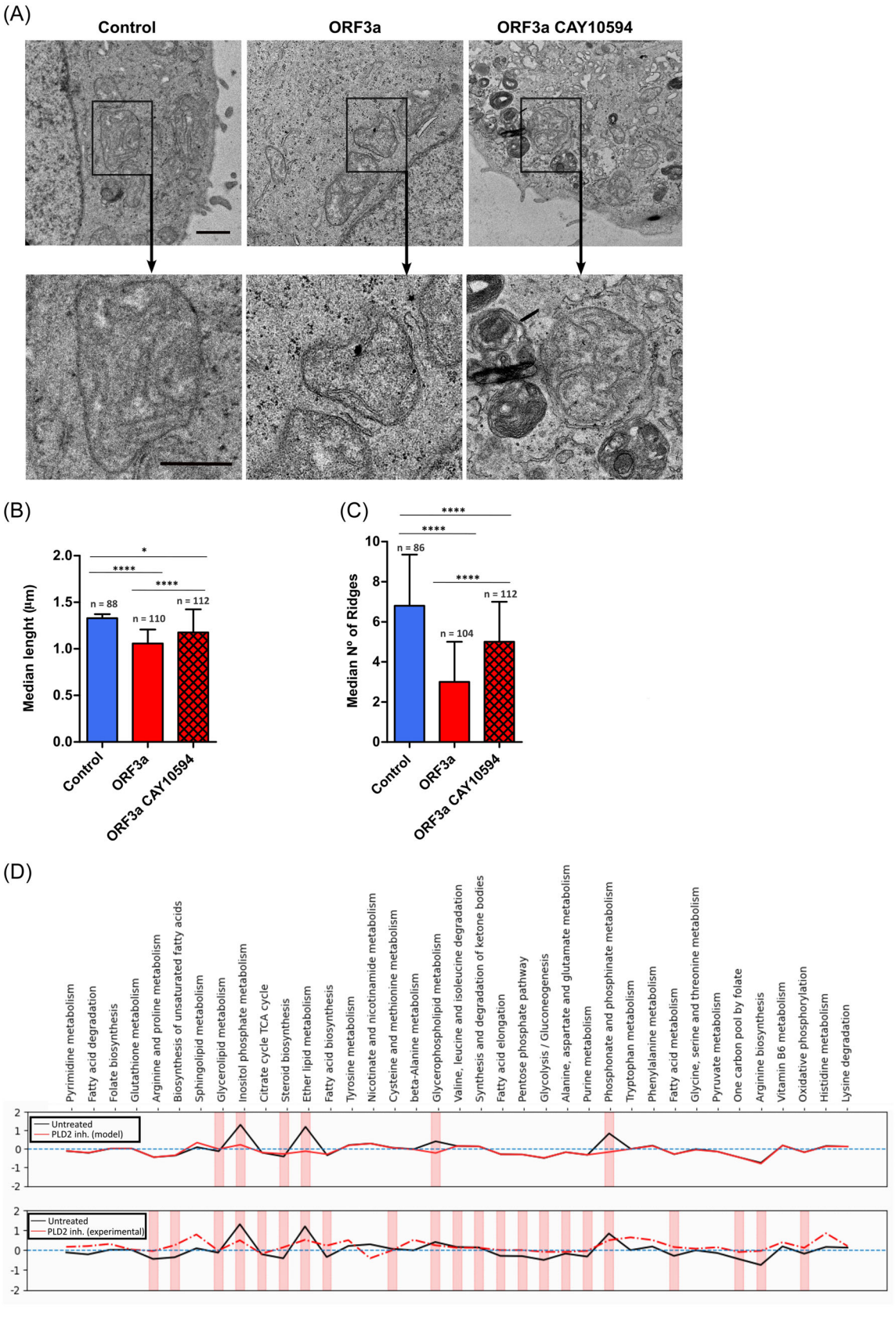

FIGURE 8 (See caption on next page).

levels of ROS, which can lead to oxidative damage and abnormal energy metabolism.[70] Other disruptions to mitochondrial activity were more prominently associated with ORF9b and ORF9c, including decreased basal and maximal respiration, spare respiratory capacity, ATP production, and basal and compensatory glycolysis. Focusing on transcriptomic data, ORF3a induced an underrepresentation of the OXPHOS pathway, which is consistent with a reduced basal respiration, maximal respiration, ATP production and proton leak associated with the expression of this viral protein. However, although we also found an underrepresentation of glycolysis pathway, we did not observed alterations in basal or compensatory glycolysis in functional assays. That might suggest a compensatory mechanism in ORF3a-A549 cells which that requires further investigation. On the other hand, ORF10 induced reduced maximal respiration and spare respiratory capacity, as well as decreased compensatory glycolysis. Our findings of diminished bioenergetics metabolism as a caused by the four accessory proteins are consistent with the known loss of cellular energy metabolism caused by SARS-CoV-2 infection,[5,27,71,72] and are in line with the recognized interactions of ORF9b, ORF9c and ORF10 with mitochondrial factors, such as TOM70, MAVS or NIX, which may result in disrupted mitochondrial functions.[13,18] Recently, ORF3c, another SARS-CoV-2 accessory protein, has been shown to also alter mitochondrial metabolism, inducing a shift from glucose to fatty acid oxidation and enhancing oxidative phosphorylation. ORF3c also increases ROS production and blocks the autophagic flux.[73]

The above metabolic reprogramming induced by these individual accessory proteins fails to explain the enhanced glycolysis acutely triggered by SARS-CoV-2 infection,[5] suggesting that it is due to the effect of other viral proteins. Applying GSEA and GSMM did not solve this issue. As mentioned above, while ORF3a-A549 cells were predicted to have a downregulation of glycolysis, experimental determination of glycolytic rates failed to show such downregulation. We speculate that compensatory mechanisms, yet to be unveiled, may regulate this process. Moreover, although our real-time functional metabolic assays demonstrated a broader range of disruptions caused by ORF9b, ORF9c and ORF10 as compared to ORF3a, GSMM predicted significant changes in energy metabolism only in association with ORF3a expression and, to a lesser degree, ORF10. In contrast to these apparently inconsistent results, other experimentally observed alterations were supported and predicted by transcriptomic and GSMM analysis, notably the correlation between altered mitochondrial cristae morphology and the downregulation of genes for critical regulators of cristae morphology and function. Morphological changes in mitochondria observed in ORF-A549 cells are in line with the proposed mechanism of SARS-CoV-2 replication, suggesting viral dsRNA subcellular localization and enrichment in host cell mitochondrion,[10,11] and the alteration of the mitochondrial and endoplasmic reticulum network to viral replication organelles formed by clusters of double-membrane vesicles (DMVs).[67,74]

The predicted upregulation of bile acid and ether lipid biosynthesis pathways triggered by ORF3a and of one-carbon, fatty acid and amino acid metabolism induced by ORF10, led us to infer potential targets for intervention to revert these metabolic perturbations. A similar approach, relying on the identification of specific KDs to an existing drug, has previously revealed candidates for COVID-19 treatment.[75,76] In our study, qMTA simulations predicted phospholipase D2 (PLD2) and phospholipase C β-1 (PLCB1) as the best targets for reverting the metabolic phenotype induced by ORF3a in A549 cells. Of note, it is reported that PLD2 augments adaptative thermogenesis by improving mitochondrial quality and quantity,[62] and phosphatidic acid, the catalytic product of PLD2, has been described as essential for SARS-CoV-2 replication.[77] as previously described,[62] we have showed that PLD inhibitor treatment was able to revert altered mitochondria morphology in ORF3a-A549 cells, and restore control cells metabolic phenotype, validating the gene knock downs (KDs) simulation obtained by our model.

In summary, we have found that the SARS-CoV-2 accessory proteins, ORF3a, ORF9b, ORF9c and ORF10, produce significant mitochondrial alterations and metabolic reprogramming in A549 lung epithelial cells. Although SARS-CoV-2 accessory proteins are considered nonessential for virus replication, our analyses suggest that, at least ORF3a, may have a direct effect on the viral life cycle, co-opting host cell lipid metabolism, possibly for DMV formation, thus ultimately impacting viral replication. Finally, we have identified putative metabolic targets that could be employed to counteract the effects of SARS-CoV-2 accessory proteins ORF3a and ORF10. Indeed, we have validated the use of CAY10594 as a PLD2 inhibitor, to revert altered metabolic phenotype induced by SARS-CoV-2 ORF3a expression. As such, this study illustrates GSMM as a viable tool for investigating the pathobiology of SARS-CoV-2 and as an aid to identify novel antiviral strategies.

4 | LIMITATIONS OF THE STUDY

This study relies on a human lung cancer cell line, with features of alveolar type 2 (AT2) lineage cells, bearing stable integration and displaying constitutive expression of a single type of viral transcript

FIGURE 8 Effect of CAY10594 treatment (PLD2 inhibitor) on ORF3a-A549 cells. (A) Comparison by transmission electron microscopy of mitochondrial appearance in control, ORF3a-A549 and ORF3a-A549 CAY10594 cells ultrathin sections. Scale bar indicates 1 µm (upper panel) and 500 nm (bottom panel). (B) Median of mitochondria longest diameter and median number of ridges per mitochondrion (C) evaluated from TEM micrographs of each cell line. * = $p < 0.05$ and **** = $p < 0.0001$. (D) Metabolic profile triggered by ORF3a accessory protein (black line, "untreated"), its reversion by GSMM-mediated *in silico* analysis (continuous red line, "PLD2 inh. (model)", upper panel), and its reversion by CAY10594 (PLD inhibitor) treatment (dashed red line, "PLD2 inh. (experimental)", bottom panel). Y axis represents log2 FC, and the dashed-horizontal blue line at each plot represents the control state (i.e., log2 FC = 0). PLD2, phospholipase D2.

and protein per cell. We recognize that this model represents a substantial departure from the circumstances of an acute SARS-CoV-2 infection, during which the entire viral genome and proteome enter susceptible cells. Interpreting features induced or suppressed by a single viral protein in our reductionist models requires caution. This is because the downregulation of cellular transcripts or proteins by one viral protein may potentially be counterbalanced by the upregulation of the same transcripts or proteins induced by a different viral protein. Nonetheless, an advantage of these models is that they enable us to acquire insights into the functions associated with specific viral genes, which can be difficult to unravel in more complex scenarios. In recognition of this potential limitation, we have placed particular emphasis on the analysis of features upregulated, rather than downregulated by viral accessory proteins, as they should contribute to phenotypes and perturbations induced also by complex virions, independent of downregulation by distinct viral factors. A further limitation, beyond complex versus reductionist approaches, stems from the long-term expression of viral proteins in our cell models, as opposed to acute viral infections, which involve short-term virus-cell interactions. The analysis of prolonged interactions reflects indirect cellular adaptations to long-term perturbations, in addition to more direct effects by the viral protein under study. However, it could be interesting for further investigations in long COVID-19 treatments. Another limitation of this study is that no validation of transcriptomic data was done, but the aim and innovation of this study was to integrate omics techniques data and functional data to simulate a GSMM that identified metabolic alterations features. Thus, certain fluxes reprogramming could have been escaped by only validating certain genes or proteins. Finally, we identify metabolic changes observed upon ORF transduction, but such alterations do not necessarily need to be beneficial for infection and viral replication and might instead be cellular responses that aim to protect against ORFs-induced cellular damage. For instance, SOD activity might protect against SARS-CoV-2-induced oxidative stress.[78]

5 | MATERIALS AND METHODS

5.1 | Cell culture, lentivirus production, and transduction

A549 pulmonary epithelial cells (ATCC CRM-CCL-185; RRID: CVCL_0023) were cultured in Dulbecco's Modified Eagle Medium (DMEM) (Gibco, #41966029) supplemented with 10% (v/v) heat-inactivated fetal bovine serum (FBS) (Gibco, #1027016), 1% Penicillin-Streptomycin (100U/ml) (Gibco, #15070063) and Amphotericin B (Gibco, #15290026). ORF3a, ORF9b, ORF9c or ORF10 accessory proteins coding sequences (codon-optimized for mammalian expression) were cloned into pLVX-EF1α-IRES-Puro Cloning and Expression Lentivector (Clontech, Takara, #631253) to generate pseudotyped lentiviral particles encoding each accessory protein of SARS-CoV-2 (Wuhan-Hu-1 isolate) at the Centro Nacional de Investigaciones Cardiovasculares (CNIC) Viral Vector Unit (ViVU) as described previously.[25,79] Accessory proteins were C-terminally 2 × Strep-tagged to check viral protein expression. A549 cells were transduced by incubating them with lentivirus at a MOI of 10 for 24 h followed by 2 µg/mL puromycin treatment to start the selection of successfully transduced cells. All cells were cultured at 37°C in a 5% CO_2, 90% humidity atmosphere.

5.2 | Strep-tag immunofluorescence, RNA isolation and sequencing

These methods were performed as previously described.[25,79]

5.3 | Real time qPCR

RNA samples (500 ng) were reverse-transcribed using qScript™ cDNA synthesis kit (Quanta Biosciences Inc., #95047), following manufacturer's instructions. Primers sequences are available in Supporting Information S4: Table 3 (Table S3). The final 15 µL PCR reaction included 2 µL of 1:5 diluted cDNA as template, 3 µL of 5x PyroTaq EvaGreen qPCR Mix Plus with ROX (Cultek Molecular Bioline, #88H24), and transcript-specific forward and reverse primers at a 20 µM final concentration. Real time PCR was carried out in a QuantStudio 12 K Flex system (Applied Biosystems) under the following conditions: 15 min at 95°C followed by 40 cycles (50 cycles to detect ORFs gene expression) of 30 s at 94°C, 30 s at 60°C (57°C in the case of ORFs) and 45 s at 72°C. Melting curve analyses were performed at the end, to ensure specificity of each PCR product. Relative expression results were calculated using GenEx6 Pro software (MultiD- Göteborg, Sweden), based on the Cq values obtained.

For detecting ORFs expression, RNA samples (1 µg) were reverse-transcribed using NZY First-Strand cDNA Synthesis Kit (nzytech, #MB12502), following manufacturer's instructions. qPCR reaction was performed using NZYSpeedy qPCR Green Master Mix (nzytech, #MB22402). Primers sequences are available in Supporting Information S4: Table 3 (Table S3). Real time PCR was carried out in LightCycler 96 (Roche) under the following conditions: 5 min at 95°C followed by 45 cycles of 20 s at 94°C, 30 s at 57°C. Melting curve analyses were performed at the end, to ensure specificity of each PCR product.

5.4 | Mitochondria analysis

5.4.1 | Transmission electron microscopy (ultrastructural analysis of Cells)

Cell monolayers were washed with PBS 1× and fixed in situ for 1 h at room temperature (RT) with 3% glutaraldehyde (EM Grade, Ted Pella INC) in PBS 1×. Fixed cells were washed three times with PBS 1×. Cell postfixation was as follows: 1 h at 4× with 1% osmium tetroxide

(Electron Microscopy Sciences) and 0,8% potassium ferricyanide in PBS, washed with PBS three times, and after dehydration in a gradient of 30% to 100% in ETOH, cells were embedded in a gradient of EtOH/LX 112 epoxy resin to 100% epoxy resin (Ladd Research). The samples were polymerized at 60°C for 2 days. Ultrathin 70 nm-thick sections were obtained with a Leica EM UC6 ultramicrotome (Leica Microsystems GmbH), transferred to collodion/carbon-coated EM grids and stained with Uranyl Acetate 5% for 20 min and Reynold's Lead Citrate for 5 min. 70 nm sections were visualized on a FEI Tecnai 12 electron microscope equipped with a LaB6 filament and operated at 100 kV. Images were recorded with a FEI Ceta digital camera at various magnifications. Median of mitochondria longest diameter was measured with ImageJ program, and median of ridges was counted in high resolution ME images. In both cases, at least 50 mitochondria were analyzed.

5.4.2 | TOM20 immunofluorescence

12,000 cells per well were seeded on a chamber slide with a removable 12 well chamber (ibidi, #81201). Cells were fixed with 4% PFA in PBS for 5 min, washed three times in PBS, and then permeabilized for 10 min with 0.1% Triton X-100 in PBS. TOM20 (abcam, ab186735) incubation was carried out for 1 h in PBS containing 3% BSA and 0.1% Triton X-100 at 1:100 dilution. Chamber slides were washed three times with PBS before Alexa 488 secondary anti-mouse antibody (Jackson, #155-546-062) incubation (1:1000 dilution). Texas Red-X phalloidin (Invitrogen, #T7471) was used as a cytoplasmic marker at 1:400, and DAPI (4'6-diamidino-2-phenylindole) (Thermo Fisher Scientific, #62248) was used as a nuclear marker at a final concentration of 1 µg/mL. After removing the chamber, the slides were mounted with FluorSave™ Reagent (Merck, #345789) and coverslips of 1.5H thickness were used.

5.4.3 | Optical microscopy

Images were acquired with a Thunder Imager Microscope (Leica Microsystems). To ensure reliable cell comparisons, only single cells were acquired to avoid differences due to cell-cell adhesion and to reduce segmentation errors. To identify single cells, we used a custom-made program named AIMS. This program uses, first, a fast-low-resolution scan (5×) to detect cells (Phalloidin - Actin) and nuclei (DAPI-DNA), and, then, an image analysis macro runs discarding objects bigger or smaller than a single cell. After this, all the coordinates for single cells localized in AIMS are loaded and acquired automatically in Thunder imager (40× HC PL APO 0.95 NA dry objective).

5.4.4 | Image analysis

To identify mitochondrial size (mitochondria fragmentation), number per cell, and area covered by mitochondria (mitochondrial mass), at least 200 cells were analyzed. Images were processed by using Cell profiler.[80] Statistical analysis was performed with SPSS v19.0 (IBM).

5.4.5 | Tracking analysis

To estimate the motility of mitochondria, 50,000 or 75,000 cells per well were seeded on a chamber slide (ibidi, #80826) and stained with MitoTracker Red. The emitted fluorescence was imaged using Thunder imager (40X HC PL APO 0.95 NA dry objective), time lapse data were recorded at 33 frame per second and field of views were randomly selected from the imaging software (Leica) across the sample. The tracking analysis was performed with TrackMate 7.[81] Due to their noncircular shape, mitochondria were identified using a mask detector. The masks were generated for each frame using a custom script. Here, we subtracted the background light in each frame via top hat filtering and evened out the fluorescence signal with a high-pass filter to avoid the misdetection of dimmer organelles at the cell borders. Finally, to reject possible lingering background signal, we generated the masks using an adaptive threshold calculated considering the local background levels. Afterwards, mitochondria motion and speed were estimated using a sparse LAP tracker.[82] To obtain more robust estimate of the average speed of each detected track, we only considered tracks with at least 20 time points.

5.4.6 | Flow cytometry

Cells were seeded at 300,000 cells/well in 6-well plates 24 h before staining. For quantitative analysis of membrane potential, cells were stained in DMEM 1% penicillin/streptomycin with 5 nM MitoView 633 (Biotium, #70055). Plates were incubated at 37°C for 30 min protected from light. Cells were then harvested, washed with PBS 1× and resuspended in PBS. For these experiments, 10,000 events were analysed using a CytoFLEX flow cytometer (Beckman Coulter) and FlowJo v10 software (BD Biosciences).

5.5 | Differential gene expression

The R/Bioconductor package DESeq. 2v.1.40.2[83] was used to evaluate the differential expression among the experimental groups (ORFs vs control). Genes for which the sum of raw counts across all of the samples was <10 were discarded. Genes with an adjusted $p \leq 0.05$ and an absolute log2 fold change ≥1 were considered differentially expressed.

5.6 | Gene set enrichment analysis

GSEAPreranked was used to assess gene enrichment compared to gene sets from the MSigDB collection (Hallmark gene sets).[84] It was

performed with 1000 random permutations and obtaining FDR q value and normalized enrichment scores (NES). Genes were ranked following the Wald statistic obtained with DESeq. 2.

5.7 | Heatmaps

The R package pheatmap v.1.0.12[85] was used to perform the heatmaps of gene expression obtained with DESeq. 2, normalized by variance stabilizing transformation (vst).

5.8 | ROS production analysis

ROS production was evaluated using the ROS Detection Assay Kit (Canvax Biotec S.L.) which contains the cell-permeant reagent dichlorodihydrofluorescein diacetate (H_2DCFDA), an indicator of reactive oxygen intermediates, that becomes fluorescent when oxidized, following the manufacturer's instructions. Cells were seeded on a 24 well plates at 75,000 cells per well 2-day prior assay. Cells were incubated with H_2DCFDA (25 mM) for 45 min at 37°C. Positive control cells were treated with 100 µM H_2O_2. ROS were measured by flow cytometry (BD Accuri C6 Plus Flow Cytometer).

5.9 | Seahorse extracellular flux analysis

Agilent Seahorse XF Cell Mito Stress Test was applied, and oxygen consumption rate (OCR) and extracellular acidification rate (ECAR) were determined using Agilent Seahorse XFe24 Analyzer (Seahorse Bioscience, Agilent) previously calibrated using Seahorse XF Calibrant solution in a CO_2-free incubator overnight. 24 h before the assay, cells were seeded at 37,500 cells per well in a Seahorse 24-well XF Cell Culture microplate in DMEM culture medium and were allowed to adhere for 24 h in 5% CO_2 atmosphere at a 37°C. On the day of assay, media was changed to XF DMEM medium supplemented with 10 mM glucose, 1 mM sodium pyruvate and 2 mM glutamine, pH 7.4, and then maintained in XF assay media at 37°C in a CO_2-free incubator 1 h. Mitochondrial function of the cells was analyzed by sequential injections of the modulators oligomycin (1 µM), carbonyl cyanide-*p*-trifluoromethoxyphenylhydrazone (FCCP, 1 µM) and a mixture of antimycin A and rotenone (Rot/AA, 0.5 µM).

For glycolytic rate analysis, the medium was changed to Seahorse XF DMEM medium (10 mM glucose, 1 mM sodium pyruvate, 2 mM glutamine, pH 7.4). Then, ECAR and OCR were recorded using the Agilent Seahorse XF24 Analyzer following injections with 0.5 µM Rot/AA and 50 mM 2-deoxyglucose (2-DG) (XF Glycolytic Rate Test Kit), respectively. Data were collected using Agilent Seahorse Wave 2.6.1 Desktop software and normalized to protein concentration determined at the end of the assay. Data were exported to GraphPad Prism version 9 for analysis.

5.10 | Measurement of consumption and production rates of metabolites

For measurement of uptake and production rates of metabolites, 200,000 cells per well were seeded in triplicate in 6-well plates with standard incubation medium. After 24 h, cells were counted and supernatants were collected and frozen until further analysis. Consumption and production rates of metabolites were determined by measuring metabolite concentration in incubation media at the beginning and at the end of 24h-incubation time and normalizing the absolute consumption/production by time and cell number assuming linear cell growth (measured rates shown in Supporting Information S3: Table 2). Glucose, lactate, glutamate and glutamine concentrations in medium aliquots were determined spectrophotometrically using NAD(P)H- coupled enzymatic reactions in an autoanalyzer Cobas Mira Plus (Horiba ABX).[86] Concentration of amino acids and biogenic amines were determined using the Absolute IDQ p180 kit from Biocrates Life Sciences (Innsbruck) and an AB Sciex 6500 QTRAP MS/MS mass spectrometer coupled to a UHPLC Agilent 1290 Infinity II System. 10 µL of media was plated in each well, and the kit was processed following manufacturer's instructions. Analyst and the MetIDQ™ software packages were used to analyse the obtained data and calculate metabolite concentrations.[86]

5.11 | Construction of condition-specific GSMMs

Condition-specific Genome-Scale Metabolic Models (GSMMs) of control and ORF-A549 cells were reconstructed using the human GSMM Recon3D[87] as a template by integrating transcriptomics (RNAseq), uptake and production rates of metabolites (measured as previously indicated) and Seahorse extracellular fluxes, using the COBRApy toolbox.[88] As part of this reconstruction, enzymes with low expression were removed from the network. More in detail, enzymes with average gene expression (FPKM) value under 1 in all conditions were removed, always ensuring their removal still allowed to produce 50% of optimal biomass and to sustain the measured rates of metabolite uptake and secretion. In addition, enzymes with FPKM values under 1 in any of the ORF-A549 cell lines, were also removed from the condition-specific model if the difference against the control was statistically significant (FDR < 0.05).

5.12 | Quadratic metabolic transformation algorithm

The metabolic transitions of ORF-A549 were simulated with the quadratic metabolic transformation algorithm (qMTA).[52] qMTA was run using as an input the condition-specific models, the reference (i.e., control) flux distribution for A549 cells and the gene expression and measured rates fold-change between control cells and ORF-A549 cells (measured rates shown in Supporting Information S3:

Table 2). The reference flux distribution was defined as the average flux values when sampling the solution space within 99% of GIME3's optimal solution[51,52] in the A549 control model (i.e., nontransduced A549 cells). Briefly, qMTA simulates the metabolic transitions of A549 when transduced with ORFs by maximizing the consistency between the variation in gene expression and measured rates and the resulting flux distribution relative to the reference flux distribution. As part of this process, p-values for differential gene expression and standard deviation for measured flux rates are used to give more weight to measured variations with a stronger statistical significance. The result is a flux distribution consistent with the transcriptomics and measured rates for each transfection, i.e., ORF3a, ORF9b, ORF9c, and ORF10 (ORF-A549 cells). To facilitate summarizing the results of the metabolic transformation, individual fluxes are assigned to a KEGG pathway. This assignment is achieved by matching the genes catalyzing each reaction to the gene-pathway annotation of KEGG. Then, the individual reaction fluxes of each pathway are added (in absolute value) to compute the total flux value for each pathway. To further summarize the results, KEGG pathways were also grouped into four metabolic pathway superfamilies (Bioenergetics and carbohydrate, amino acids, lipids and nucleotide metabolism) and the total flux value for each superfamily was calculated using the same procedure.

5.13 | Identification of targets disrupting metabolic transformations

qMTA is also used to identify putative gene knock downs and metabolic inhibitors that can disrupt the metabolic transformation underlying ORF transduction. This is achieved for each condition by iteratively repeating the qMTA analysis with gene knock downs (simulated by reducing the maximum flux to each mapped reaction to 50% of the control condition). This tests the capacity of a gene knock down to prevent or disrupt the metabolic transformation. To increase robustness,[89] this analysis is complemented by using the minimization of metabolic adjustment (MOMA) algorithm[90] to simulate the capacity of individual gene knock downs to switch the ORF metabolic flux distribution to a state closer to the A549 control cells. Briefly, MOMA simulates the effect of a gene knock down by reducing the maximum flux to each reaction mapped to the gene to 50% and minimizing the variation in the remaining reactions. For each condition, putative gene knock downs are ranked based on their capacity to both disrupt the metabolic transformation from control to ORF-A549 cells and their capacity to revert the ORF-transduced state to the control.

5.14 | CAY10594 treatment (PLD2 inhibitor)

A549 control and ORF3a-A549 cells were seeded at 300,000 cells/well in 6-well plates 24 h before treatment. Medium containing the PLD2-selective inhibitor, CAY10594 (1 μM), was added to cells for an additional 24 h. For the transcriptomic analysis, NGS experiments were performed in the Genomics Unit of the CNIC (Madrid, Spain). Transmission electron microscopy was performed as described in "Transmission Electron Microscopy (Ultrastructural Analysis of Cells)", but sections were visualized on a JEOL 1230 electron microscope operated at 80 kV, and mages were recorded with a TVIPS CMOS 4 K camera. Median of mitochondria longest diameter was measured with ImageJ program, and median of ridges was counted in high resolution ME images. In both cases, at least 86 mitochondria were analyzed in control cells, and 100 mitochondria in ORF3a-A549 cells. The flux distribution for ORF3a-A549 cells treated with CAY10594, consistent with the transcriptomics analysis, has been computed from the reconstructed treatment-specific GSMM as described above.

AUTHOR CONTRIBUTIONS

Conceptualization: María Montoya. *Methodology*: All authors. *Investigation*: All authors. *Funding acquisition*: María Montoya, Juan J. Garrido, and Marta Cascante. *Writing—original draft*: María Montoya, Blanca D. López-Ayllón, Juan J. Garrido, Marta Cascante and Timothy M. Thomson. *Writing—review and editing*: María Montoya, Timothy M. Thomson, Blanca D. López-Ayllón.

ACKNOWLEDGMENTS

We would like to thank the CCiTUB (Scientific and Technological Centers of the UB) of the Universitat de Barcelona (Barcelona, Spain), for the expert and technical help using the LC-MS/MS equipment, and Dr. Marian Oliva for the critical review of the manuscript. This research work was funded by the European Commission–NextGenerationEU (Regulation EU 2020/2094), through CSIC's Global Health Platform (PTI+ Salud Global) (COVID-19-117 and SGL2103015), Junta de Andalucía (CV20-20089), Spanish Ministry of Science project (PID2021-123399OB-I00), the Agency for Management of University and Research Grants from Generalitat de Catalunya-AGAUR (2020PANDE00048 and 2021SGR00350) and ICREA foundation (ICREA-Academia-2021 to MC) of Generalitat de Catalunya, and an AESi grant of the Instituto de Salud Carlos III (PI20CIII-00014). SM is Serra Húnter Fellow. TGG is recipient of a Ramón y Cajal contract funded by MCIN/AEU/10.13039/501100011033 and NextGeneration EU/PRTR.

CONFLICT OF INTEREST STATEMENT

The authors declare no conflict of interest.

DATA AVAILABILITY STATEMENT

The datasets generated during the current study are available in the NCBI BioProject database (https://www.ncbi.nlm.nih.gov/bioproject/) under accession number PRJNA975806 for ORF3a-A549 cells, PRJNA946640 for ORF9b and ORF9c transduced cells, PRJNA 976185 for ORF10-A549 cells, and PRJNA841835 for A549 control cells.

ORCID

Raúl Fernández-Rodríguez http://orcid.org/0000-0001-8301-0244
Timothy M. Thomson http://orcid.org/0000-0002-4670-9440

REFERENCES

1. World Health Organization. WHO Coronavirus (COVID-19) Dashboard. (2023).
2. Cheng K, Martin-Sancho L, Pal LR, et al. Genome-scale metabolic modeling reveals SARS-CoV-2-induced metabolic changes and antiviral targets. *Mol Syst Biol*. 2021;17:e10260. doi:10.15252/msb.202110260
3. Pei R, Feng J, Zhang Y, et al. Host metabolism dysregulation and cell tropism identification in human airway and alveolar organoids upon SARS-CoV-2 infection. *Protein Cell*. 2021;12:717-733.
4. Gardinassi LG, Souza COS, Sales-Campos H, Fonseca SG. Immune and metabolic signatures of COVID-19 revealed by transcriptomics data reuse. *Front Immunol*. 2020;11:1636. doi:10.3389/fimmu.2020.01636
5. Guarnieri JW, Dybas JM, Fazelinia H, et al. Core mitochondrial genes are down-regulated during SARS-CoV-2 infection of rodent and human hosts. *Sci Transl Med*. 2023;15:eabq1533.
6. Ehrlich A, Ioannidis K, Nasar M, et al. Efficacy and safety of metabolic interventions for the treatment of severe COVID-19: in vitro, observational, and non-randomized open-label interventional study. *eLife*. 2023;12:e79946. doi:10.7554/eLife.79946
7. Pérez-Torres I, Guarner-Lans V, Soria-Castro E, et al. Alteration in the lipid profile and the desaturases activity in patients with severe pneumonia by SARS-CoV-2. *Front Physiol*. 2021;12:667024.
8. Singh K, Chen YC, Hassanzadeh S, et al. Network analysis and transcriptome profiling identify autophagic and mitochondrial dysfunctions in SARS-CoV-2 infection. *Front Genet*. 2021;12:599261.
9. Nardacci R, Colavita F, Castilletti C, et al. Evidences for lipid involvement in SARS-CoV-2 cytopathogenesis. *Cell Death Dis*. 2021;12:263.
10. Bhowal C, Ghosh S, Ghatak D, De R. Pathophysiological involvement of host mitochondria in SARS-CoV-2 infection that causes COVID-19: a comprehensive evidential insight. *Mol Cell Biochem*. 2023;478(6):1325-1343. doi:10.1007/s11010-022-04593-z
11. Shang C, Liu Z, Zhu Y, et al. SARS-CoV-2 causes mitochondrial dysfunction and mitophagy impairment. *Front Microbiol*. 2021;12:780768.
12. Lee YK, Lee JA. Role of the mammalian ATG8/LC3 family in autophagy: differential and compensatory roles in the spatiotemporal regulation of autophagy. *BMB Rep*. 2016;49:424-430.
13. Li X, Hou P, Ma W, et al. SARS-CoV-2 ORF10 suppresses the antiviral innate immune response by degrading MAVS through mitophagy. *Cell Mol Immunol*. 2022;19:67-78.
14. West AP, Shadel GS, Ghosh S. Mitochondria in innate immune responses. *Nat Rev Immunol*. 2011;11:389-402.
15. Burtscher J, Cappellano G, Omori A, Koshiba T, Millet GP. Mitochondria: in the cross fire of SARS-CoV-2 and immunity. *iScience*. 2020;23:101631.
16. Redondo N, Zaldívar-López S, Garrido JJ, Montoya M. SARS-CoV-2 accessory proteins in viral pathogenesis: knowns and unknowns. *Front Immunol*. 2021;12:708264.
17. Hurtado-Tamayo J, Requena-Platek R, Enjuanes L, Bello-Perez M, Sola I. Contribution to pathogenesis of accessory proteins of deadly human coronaviruses. *Front Cell Infect Microbiol*. 2023;13:1166839.
18. Gao X, Zhu K, Qin B, Olieric V, Wang M, Cui S. Crystal structure of SARS-CoV-2 Orf9b in complex with human TOM70 suggests unusual virus-host interactions. *Nat Commun*. 2021;12:2843.
19. Zhou Y, Liu Y, Gupta S, et al. A comprehensive SARS-CoV-2–human protein–protein interactome reveals COVID-19 pathobiology and potential host therapeutic targets. *Nature Biotechnol*. 2023;41:128-139.
20. Ren Y, Shu T, Wu D, et al. The ORF3a protein of SARS-CoV-2 induces apoptosis in cells. *Cell Mol Immunol*. 2020;17:881-883.
21. Wang R, Yang X, Chang M, et al. ORF3a protein of severe acute respiratory syndrome coronavirus 2 inhibits interferon-activated Janus kinase/signal transducer and activator of transcription signaling via elevating suppressor of cytokine signaling 1. *Front Microbiol*. 2021;12:752597.
22. Miller AN, Houlihan PR, Matamala E, et al. The SARS-CoV-2 accessory protein Orf3a is not an ion channel, but does interact with trafficking proteins. *eLife*. 2023;12:e84477. doi:10.7554/eLife.84477
23. Han L, Zhuang MW, Deng J, et al. SARS-CoV-2 ORF9b antagonizes type I and III interferons by targeting multiple components of the RIG-I/MDA-5-MAVS, TLR3-TRIF, and cGAS-STING signaling pathways. *J Med Virol*. 2021;93:5376-5389.
24. Gordon DE, Jang GM, Bouhaddou M, et al. A SARS-CoV-2 protein interaction map reveals targets for drug repurposing. *Nature*. 2020;583:459-468.
25. López-Ayllón BD, de Lucas-Rius A, Mendoza-García L, et al. SARS-CoV-2 accessory proteins involvement in inflammatory and profibrotic processes through IL11 signaling. *Front Immunol*. 2023;14:1220306.
26. Bhowal C, Ghosh S, Ghatak D, De R. Pathophysiological involvement of host mitochondria in SARS-CoV-2 infection that causes COVID-19: a comprehensive evidential insight. *Mol Cell Biochem*. 2023;478:1325-1343.
27. Ramachandran K, Maity S, Muthukumar AR, et al. SARS-CoV-2 infection enhances mitochondrial PTP complex activity to perturb cardiac energetics. *iScience*. 2022;25:103722.
28. Miserey-Lenkei S, Trajkovic K, D'Ambrosio JM, et al. A comprehensive library of fluorescent constructs of SARS-CoV-2 proteins and their initial characterisation in different cell types. *Biol Cell*. 2021;113:311-328.
29. Dominguez Andres A, Feng Y, Rosa Campos A, et al. SARS-CoV-2 ORF9c is a membrane-associated protein that suppresses antiviral responses in cells. *bioRxiv*. 2020.
30. Han L, Zheng Y, Deng J, et al. SARS-CoV-2 ORF10 antagonizes STING-dependent interferon activation and autophagy. *J Med Virol*. 2022;94:5174-5188.
31. Subramanian A, Tamayo P, Mootha VK, et al. Gene set enrichment analysis: a knowledge-based approach for interpreting genome-wide expression profiles. *Proc Nat Acad Sci*. 2005;102:15545-15550.
32. Sciuto KJ, Deng SW, Moreno A, Zaitsev AV. Chronology of critical events in neonatal rat ventricular myocytes occurring during reperfusion after simulated ischemia. *PLoS One*. 2019;14:e0212076.
33. Jeyaraju DV, Cisbani G, Pellegrini L. Calcium regulation of mitochondria motility and morphology. *Biochim et Biophys Act Bioenergetics*. 2009;1787:1363-1373.
34. Miller KE, Sheetz MP. Axonal mitochondrial transport and potential are correlated. *J Cell Sci*. 2004;117:2791-2804.
35. Caron C, Bertolin G. Cristae shaping and dynamics in mitochondrial function. *J Cell Sci*. 2024;137:jcs260986. doi:10.1242/jcs.260986
36. Gao S, Hu J. Mitochondrial fusion: the machineries in and out. *Trends Cell Biol*. 2021;31:62-74.
37. Chen W, Zhao H, Li Y. Mitochondrial dynamics in health and disease: mechanisms and potential targets. *Signal Transduct Target Ther*. 2023;8:333.
38. Mozdy AD, McCaffery JM, Shaw JM. Dnm1p GTPase-mediated mitochondrial fission is a multi-step process requiring the novel integral membrane component Fis1p. *J Cell Biol*. 2000;151:367-380.
39. Nolden KA, Harwig MC, Hill RB. Human Fis1 directly interacts with Drp1 in an evolutionarily conserved manner to promote mitochondrial fission. *J Biol Chem*. 2023;299:105380.

40. Wang S, Tan J, Miao Y, Zhang Q. Mitochondrial dynamics, mitophagy, and mitochondria-endoplasmic reticulum contact sites crosstalk under hypoxia. *Front Cell Dev Biol*. 2022;10:848214.
41. Otera H, Wang C, Cleland MM, et al. Mff is an essential factor for mitochondrial recruitment of Drp1 during mitochondrial fission in mammalian cells. *J Cell Biol*. 2010;191:1141-1158.
42. Shen Q, Yamano K, Head BP, et al. Mutations in Fis1 disrupt orderly disposal of defective mitochondria. *Mol Biol Cell*. 2014;25:145-159.
43. Palmer CS, Osellame LD, Laine D, Koutsopoulos OS, Frazier AE, Ryan MT. MiD49 and MiD51, new components of the mitochondrial fission machinery. *EMBO Rep*. 2011;12:565-573.
44. Losón OC, Song Z, Chen H, Chan DC. Fis1, Mff, MiD49, and MiD51 mediate Drp1 recruitment in mitochondrial fission. *Mol Biol Cell*. 2013;24:659-667.
45. Palmer CS, Elgass KD, Parton RG, Osellame LD, Stojanovski D, Ryan MT. Adaptor proteins MiD49 and MiD51 can act independently of Mff and Fis1 in Drp1 recruitment and are specific for mitochondrial fission. *J Biol Chem*. 2013;288:27584-27593.
46. Osellame LD, Singh AP, Stroud DA, et al. Cooperative and independent roles of the Drp1 adaptors Mff, MiD49 and MiD51 in mitochondrial fission. *J Cell Sci*. 2016;129:2170-2181.
47. Liu R, Chan DC. The mitochondrial fission receptor Mff selectively recruits oligomerized Drp1. *Mol Biol Cell*. 2015;26:4466-4477.
48. Koirala S, Guo Q, Kalia R, et al. Interchangeable adaptors regulate mitochondrial dynamin assembly for membrane scission. *Proc Nat Acad Sci*. 2013;110:E1342-E1351.
49. Venditti P, Di Meo S. The role of reactive oxygen species in the life cycle of the mitochondrion. *Int J Mol Sci*. 2020;21:2173.
50. Viale A, Pettazzoni P, Lyssiotis CA, et al. Oncogene ablation-resistant pancreatic cancer cells depend on mitochondrial function. *Nature*. 2014;514:628-632.
51. Schmidt BJ, Ebrahim A, Metz TO, Adkins JN, Palsson BØ, Hyduke DR. GIM3E: condition-specific models of cellular metabolism developed from metabolomics and expression data. *Bioinformatics*. 2013;29:2900-2908.
52. Foguet C, Xu Y, Ritchie SC, et al. Genetically personalised organ-specific metabolic models in health and disease. *Nat Commun*. 2022;13:7356.
53. Blanco-Melo D, Nilsson-Payant BE, Liu WC, et al. Imbalanced host response to SARS-CoV-2 drives development of COVID-19. *Cell*. 2020;181:1036-1045.e9. e1039.
54. Daniloski Z, Jordan TX, Wessels HH, et al. Identification of required host factors for SARS-CoV-2 infection in human cells. *Cell*. 2021;184:92-105.e16.e116.
55. Li Y, Renner DM, Comar CE, et al. SARS-CoV-2 induces double-stranded RNA-mediated innate immune responses in respiratory epithelial-derived cells and cardiomyocytes. *Proc Nat Acad Sci*. 2021;118:e2022643118. doi:10.1073/pnas.2022643118
56. Blunsom NJ, Cockcroft S. CDP-diacylglycerol synthases (CDS): gateway to phosphatidylinositol and cardiolipin synthesis. *Front Cell Dev Biol*. 2020;8:63.
57. Li X, Tang L, Deng J, et al. Identifying metabolic reprogramming phenotypes with glycolysis-lipid metabolism discoordination and intercellular communication for lung adenocarcinoma metastasis. *Commun Biol*. 2022;5:198.
58. Brocker C, Lassen N, Estey T, et al. Aldehyde dehydrogenase 7A1 (ALDH7A1) is a novel enzyme involved in cellular defense against hyperosmotic stress. *J Biol Chem*. 2010;285:18452-18463.
59. Schliess F, Görg B, Häussinger D. Pathogenetic interplay between osmotic and oxidative stress: the hepatic encephalopathy paradigm. *Biol Chem*. 2006;387:1363-1370.
60. Thakur R, Naik A, Panda A, Raghu P. Regulation of membrane turnover by phosphatidic acid: cellular functions and disease implications. *Front Cell Dev Biol*. 2019;7:83.
61. Saud Z, Tyrrell VJ, Zaragkoulias A, et al. The SARS-CoV2 envelope differs from host cells, exposes procoagulant lipids, and is disrupted in vivo by oral rinses. *J Lipid Res*. 2022;63:100208.
62. Kim HS, Park MY, Yun NJ, et al. Targeting PLD2 in adipocytes augments adaptive thermogenesis by improving mitochondrial quality and quantity in mice. *J Exp Med*. 2022;219:e20211523. doi:10.1084/jem.20211523
63. Alqutami F, Senok A, Hachim M. COVID-19 transcriptomic Atlas: a comprehensive analysis of COVID-19 related transcriptomics datasets. *Front Genet*. 2021;12:755222. doi:10.3389/fgene.2021.755222
64. Cogliati S, Frezza C, Soriano ME, et al. Mitochondrial cristae shape determines respiratory chain supercomplexes assembly and respiratory efficiency. *Cell*. 2013;155:160-171.
65. Frezza C, Cipolat S, Martins de Brito O, et al. OPA1 controls apoptotic cristae remodeling independently from mitochondrial fusion. *Cell*. 2006;126:177-189.
66. Pfanner N, van der Laan M, Amati P, et al. Uniform nomenclature for the mitochondrial contact site and cristae organizing system. *J Cell Biol*. 2014;204:1083-1086.
67. Cortese M, Lee JY, Cerikan B, et al. Integrative imaging reveals SARS-CoV-2-induced reshaping of subcellular morphologies. *Cell Host Microbe*. 2020;28:853-866.e5.e855.
68. Yapa NMB, Lisnyak V, Reljic B, Ryan MT. Mitochondrial dynamics in health and disease. *FEBS Lett*. 2021;595:1184-1204. https://doi.org/10.1002/1873-3468.14077
69. Ott C, Ross K, Straub S, et al. Sam50 functions in mitochondrial intermembrane space bridging and biogenesis of respiratory complexes. *Mol Cell Biol*. 2012;32:1173-1188.
70. Zorov DB, Juhaszova M, Sollott SJ. Mitochondrial reactive oxygen species (ROS) and ROS-induced ROS release. *Physiol Rev*. 2014;94:909-950.
71. Saleh J, Peyssonnaux C, Singh KK, Edeas M. Mitochondria and microbiota dysfunction in COVID-19 pathogenesis. *Mitochondrion*. 2020;54:1-7.
72. Singh KK, Chaubey G, Chen JY, Suravajhala P. Decoding SARS-CoV-2 hijacking of host mitochondria in COVID-19 pathogenesis. *Am J Physiol Cell Physiol*. 2020;319:C258-C267.
73. Mozzi A, Oldani M, Forcella ME, et al. SARS-CoV-2 ORF3c impairs mitochondrial respiratory metabolism, oxidative stress, and autophagic flux. *iScience*. 2023;26:107118.
74. Wolff G, Limpens RWAL, Zevenhoven-Dobbe JC, et al. A molecular pore spans the double membrane of the coronavirus replication organelle. *Science*. 2020;369:1395-1398.
75. Su J, Shen S, Hu Y, et al. SARS-CoV-2 ORF3a inhibits cGAS-STING-mediated autophagy flux and antiviral function. *J Med Virol*. 2023;95:e28175.
76. Krishnakumar R, Chen AF, Pantovich MG, et al. FOXD3 regulates pluripotent stem cell potential by simultaneously initiating and repressing enhancer activity. *Cell Stem Cell*. 2016;18:104-117.
77. Tabata K, Prasad V, Paul D, et al. Convergent use of phosphatidic acid for hepatitis C virus and SARS-CoV-2 replication organelle formation. *Nat Commun*. 2021;12:7276.
78. Mo LH, Luo XQ, Ma K, et al. Superoxide dismutase prevents SARS-CoV-2-induced plasma cell apoptosis and stabilizes specific antibody induction. *Oxid Med Cell Longevity*. 2022;2022:5397733.
79. García-García T, Fernández-Rodríguez R, Redondo N, et al. Impairment of antiviral immune response and disruption of cellular functions by SARS-CoV-2 ORF7a and ORF7b. *iScience*. 2022;25:105444.
80. Stirling DR, Swain-Bowden MJ, Lucas AM, Carpenter AE, Cimini BA, Goodman A. CellProfiler 4: improvements in speed, utility and usability. *BMC Bioinformatics*. 2021;22:433.
81. Ershov D, Phan MS, Pylvänäinen JW, et al. TrackMate 7: integrating state-of-the-art segmentation algorithms into tracking pipelines. *Nature Methods*. 2022;19:829-832.

82. Jaqaman K, Loerke D, Mettlen M, et al. Robust single-particle tracking in live-cell time-lapse sequences. *Nat Methods*. 2008;5:695-702.
83. Love MI, Huber W, Anders S. Moderated estimation of fold change and dispersion for RNA-seq data with DESeq. 2. *Genome Biol*. 2014;15:550.
84. Liberzon A, Birger C, Thorvaldsdóttir H, Ghandi M, Mesirov JP, Tamayo P. The molecular signatures database hallmark gene set collection. *Cell Systems*. 2015;1:417-425.
85. Kolde R Implementation of heatmaps that offers more control over dimensions and appearance. 2019. https://CRAN.R-project.org/package=pheatmap
86. de Atauri P, Benito A, Vizán P, et al. Carbon metabolism and the sign of control coefficients in metabolic adaptations underlying k-ras transformation. *Biochim et Biophys Act Bioenergetics*. 2011;1807:746-754.
87. Brunk E, Sahoo S, Zielinski DC, et al. Recon3D enables a three-dimensional view of gene variation in human metabolism. *Nat Biotechnol*. 2018;36:272-281.
88. Ebrahim A, Lerman JA, Palsson BO, Hyduke DR. COBRApy: COnstraints-based reconstruction and analysis for python. *BMC Syst Biol*. 2013;7:74.
89. Valcárcel LV, Torrano V, Tobalina L, Carracedo A, Planes FJ. rMTA: robust metabolic transformation analysis. *Bioinformatics*. 2019;35:4350-4355.
90. Segrè D, Vitkup D, Church GM. Analysis of optimality in natural and perturbed metabolic networks. *Proc Nati Acad Sci*. 2002;99:15112-15117.

SUPPORTING INFORMATION

Additional supporting information can be found online in the Supporting Information section at the end of this article.

How to cite this article: López-Ayllón BD, Marin S, Fernández MF, et al. Metabolic and mitochondria alterations induced by SARS-CoV-2 accessory proteins ORF3a, ORF9b, ORF9c and ORF10. *J Med Virol*. 2024;96:e29752. doi:10.1002/jmv.29752